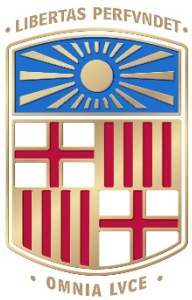

UNIVERSITAT DE BARCELONA

Final Degree Project

Biomedical Engineering Degree

"Preprocessing and decoding neural traces of serial biases in working memory from intracranial electrophysiological recordings in humans"

Barcelona, 11th of June 2025

Author: Alberto Hurtado

Directors: Albert Compte

& Alexis Pérez

ACKNOWLEDGMENTS

This thesis would not have been possible without the support of many people. I am deeply grateful to Albert Compte for giving me the opportunity to be a part of this research and for his mentorship and encouragement, and to Daniel Pacheco, whose help in iEEG cleaning has brought us to where we are now.

Additionally, I wanted to express my gratitude to the Hospital Clinic and its Unit of Epilepsy, who allowed us to work closely with them and collect data. Most of all, I am deeply thankful to the patients who collaborated and made this research possible.

I am also especially grateful to Dr. Roldán, whose assistance in providing patient information (MRI sequences, CT scans, and surgical planning details) was fundamental to this study.

Furthermore, I would like to thank my professors, whose guidance and knowledge have shaped my academic journey, and my family and friends, who have been my source of support and encouragement throughout this process. Their patience, belief in me, and motivation have been of much help in completing this thesis.

Finally, I would like to express my deepest gratitude to Alexis Pérez, whose mentorship, guidance, and support have been invaluable throughout this research. His patience, expertise, and willingness to help at every step of the analysis have made a significant impact on this work. I am truly grateful for his dedication and for everything I have learned from him during this journey.

ABSTRACT

Working memory is a fundamental cognitive process enabling short-term maintenance and manipulation of information. In recent years, behavioral studies have revealed biases affecting working memory contents. It has been observed that information maintained in our working memory buffer (e.g., spatial location, color, auditory frequency) shifts towards previously observed positions, an effect known as serial dependency bias, and its magnitude correlates with conditions as schizophrenia and NMDAR encephalitis. This project sought to characterize the neural correlates of working memory and serial dependency biases using intracranial electroencephalography (iEEG), an invasive technique with high temporal and spatial resolution. Nevertheless, iEEG analyses present several challenges associated with the signal's nature that need addressing. In this TFG, multiple artifact detection and cleaning methods were developed and evaluated on two criteria: how many trials and electrodes it preserved, and how accurately it detected current trial information and serial biases from preceding trials. The custom automated approach provided marginally higher decoding accuracy at the cost of greater data loss, whereas the manual cleaning delivered equivalent performance while preserving more data, rendering it preferable for whole-brain analyses. After artifact removal, multiple analyses confirmed that information regarding both current stimuli and past trials could be decoded from distributed iEEG patterns. Although limited by a small epilepsy cohort, these findings offer practical guidance for future iEEG studies by demonstrating the trade-offs between data preservation and signal clarity and suggesting that serial dependency signals may be distributed across brain regions. This project represents the first investigation of working memory's mechanisms using human iEEG.

Key words: Intracranial electroencephalography, electrophysiological signal preprocessing, artifact detection, serial dependencies, neural decoding, working memory.

RESUM

La memòria de treball és un procés cognitiu que permet el manteniment i manipulació d'informació a curta durada. Recentment, estudis conductuals han revelat biaixos que afecten continguts de la memòria de treball. S'ha observat que la informació mantinguda al nostre buffer de memòria de treball (localització espacial, color, freqüència auditiva) es desplaça cap a posicions observades prèviament, un efecte conegut com a biaix de dependència serial, i la seva magnitud correlaciona amb condicions com esquizofrènia i encefalitis per NMDAR. Aquest projecte pretenia caracteritzar correlats neurals de memòria de treball i biaixos de dependència serial utilitzant electroencefalografia intracranial (iEEG), una tècnica invasiva amb alta resolució temporal i espacial. Tanmateix, els anàlisis d'iEEG presenten diversos reptes associats amb la naturalesa del senyal. En aquest TFG, es van desenvolupar i avaluar múltiples mètodes de detecció i neteja d'artefactes segons dos criteris: quants assajos i elèctrodes preservava, i amb quina precisió detectava informació de l'assaig actual i biaixos serials d'assajos precedents. L'enfocament semiautomàtic proporcionà precisió de decodificació marginalment superior a costa de major pèrdua de dades, mentre que la neteja manual oferí rendiment equivalent preservant més dades, resultant preferible per anàlisis de cervell complet. Després de l'eliminació d'artefactes, múltiples anàlisis confirmaren que es podia decodificar informació sobre estímuls actuals i assajos passats de patrons d'iEEG distribuïts. Malgrat les limitacions d'una petita cohort d'epilèpsia, aquests resultats ofereixen orientació pràctica per futurs estudis d'iEEG demostrant compromisos entre preservació de dades i claredat del senyal, i suggereixen que els senyals de dependència serial poden estar distribuïts en regions cerebrals.

Paraules clau: Electroencefalografia intracranial, preprocessament de senyals electrofisiològics, detecció d'artefactes, dependències serials, decodificació neural, memòria de treball.

LIST OF FIGURES

LIST OF TABLES

LIST OF EQUATIONS

GLOSSARY OF ABREVIATIONS

iEEG – Intracranial Electroencephalogram

IDIBAPS – Institut d'Investigacions Biomèdiques August Pi I Sunyer

GNM – Global Neuroscience Market

ITI – Inter-Trial Interval

MRI – Magnetic Resonance Imaging

CT – Computed tomography

AC – Alternating Current

GUI – Graphical User Interface

IIR – Infinite Impulse Response

FIR – Finite Impulse Response

REST – Reference Electrode Standardization Technique

ICA – Independent Component Analysis

RANSAC – Random Sample Consensus

EDF – European Data Format

PERT – Program Evaluation and Review Technique

WBS – Work Breakdown Structure

BIDS – Brain Imaging Data Structure

SNR – Signal-to-Noise Ratio

STD – Standard Deviation

MAD – Median Absolute Deviation

PSD – Power Spectral Density

FFT – Fast Fourier Transform

DFT – Discrete Fourier Transform

ROI – Region of Interest

TABLE OF CONTENTS

1. INTRODUCTION

Despite decades of research, the human brain continues to elude comprehensive characterization, and no artificial project has yet replicated its integrative cognitive capacities. As James D. Watson once said: “The brain is the last and grandest biological frontier, the most complex thing we have yet discovered in our universe.”

Modern neuroscience has made significant advances allowing for a better understanding of mental processes from a scientific point of view, although, its societal impact remains constrained by the challenge of harmonizing and reconciling our humanity and essence together with the way of work of the brain [1].

Initially, Aristoteles explained how the brain was a radiator that kept the heart from overheating, in the 16th century the first sketch of the nervous system was created by Andreas Vesalius, but it was not until the early 1900s that Santiago Ramón y Cajal and Camillo Golgi identified the neurons as the building blocks of the brain, even showing that there exist different types [2].

Research over the past century, specially within cognitive psychology, has helped explaining and characterizing various cognitive processes that support human intelligence, including attention, perception, learning and memory. Progress in neuroimaging techniques has further elevated cognitive and systems neuroscience by providing increasingly detailed descriptions of how these processes are incorporated in the brain. Among these cognitive functions, memory stands out as particularly inclined to such integrative study, since it combines both neural dynamics and observable behavioral outcomes. Within the broader domain of memory, this work will focus on working memory: a cognitive system accountable for the temporary storage and manipulation of information necessary for tasks ranging from simple calculations to complex problem solving, and its capacity correlates with measures of humane intelligence.

Recent work has demonstrated that working memory representations are influenced by previous information held in the memory, in other words, current mnemonic content is biased toward past contents. Whitney and Fischer (2014) provided empirical support by presenting participants with a series of stimuli and observing how their reports were consistently drawn toward features of earlier items. These history-dependent distortions, often termed as serial dependency biases, may degrade working memory fidelity, but are thought to serve as an adaptative function which stabilize our interpretation of environmental stimuli, and exploit the natural temporal correlation of sensory events integrating what we perceived in the past with what we are perceiving right now.

This thesis will start off by reviewing notable findings and theoretical foundations related to working memory, and it will be followed by the findings obtained during the empirical research. This research aims to investigate the neural bases of serial biases, as they have been linked to mental disorders. We know that electrophysiological markers of these biases can be found in EEG signals, but it remains unclear whether specialized brain regions exist for this function in humans, to address this gap, this work will employ iEEG signals. Although iEEG affords exceptional temporal and spatial resolution compared to scalp recordings, it is quite vulnerable to a range of signal quality issues: high-amplitude stimulation or movement-related artifacts, line noise, electrode impedance

fluctuations and common noise between contacts, and nonstationary drifts can cover genuine neural activity [3]. Since reliable measurements and analyses of iEEG require exceptionally clear neural signals, this thesis will mostly focus on developing and comparing multiple preprocessing pipelines for artifact rejection while preserving as much data as possible. After determining the optimal cleaning strategy, human intracranial recordings will be shortly analyzed to corroborate that serial biases can also be found from inside the human brain.

A better understanding of the mechanisms behind working memory can help in educational practice, developing new treatments for cognitive disorders, and extending the theoretical understanding of human cognition. The brain indeed boggles the mind, serving as a reminder of the endless possibilities that lie when curiosity and innovation are combined.

1.1. Motivation

This project starts off from the research done by Compte Lab based on working memory. Thanks to the collaboration of IDIBAPS with the epilepsy unit led by Dr. Mar Carreño at the Hospital Clinic, we can get intracranial EEG measurements from patients suffering from epilepsy. Up to this moment, serial biases have been studied through scalp EEG in humans and intracranial EEG in monkeys. Thereby, this is an incredible opportunity which will allow us to get a far better understanding in the working memory and its serial biases. However, iEEG are notoriously susceptible to noise and artifacts as explained earlier, consequently, the principal aim of this work is to identify and validate the preprocessing strategy that maximizes the trade-off between data retention and artifact rejection. Establishing such pipeline is not only a technical exercise but also a fundamental prerequisite to accurately map cortical circuits integrating both current and past stimuli [3]. By refining artifact detection and signal cleaning, this research will both advance theoretical models of working memory and lay the groundwork to target cognitive deficits linked to serial biases in clinical populations.

1.2. Objectives

The study will be organized in three objectives closely related one to another that address both methodological and mechanistic gaps in our understanding of working memory. The first aim concerns the preprocessing of iEEG recordings, which lacks a consensus on whether non conservative artifact removal or minimal filtering yields the most faithful representation of neural signals. To solve this debate, we will implement a simple manual cleaning function that depends on the researcher expertise in detecting artifacts, a semi-automatic pipeline, and a fully automated algorithm, which will all be compared allowing us to quantify the impact of each approach on signal quality and posterior analyses. The second aim is to establish the presence neural correlates of serial biases in human intracranial measurements using different information decoding techniques. Building on these foundations, the third and final objective is to set a solid groundwork to localize the brain regions that support working memory and serial biases in humans. Altogether, these objectives will refine iEEG preprocessing methodology and show how our past experiences flow through the brain, shaping each moment of thought.

1.3. Limitations

To conduct this research, a few limitations were determined:

- As a first limitation, it is important to acknowledge that the data obtained in the iEEG comes from patients hospitalized due to an epilepsy treatment. We are lucky enough to be able to talk to them and obtain measurements, but all electrodes placed in the brain are implanted in a strategic location because of previous suspicion that the corresponding section is causing the seizures. This means that the data will not be as clean as desired, and a previous filtering process will need to be applied so that we can extract the best measurements possible from all channels and the location of serial biases in the brain will be influenced too. As an added limitation to data, environmental conditions must be mentioned since they are not controllable and may add variability to the data. To try to fix this, the experiment shall be always observed so that notes can be taken if necessary for post-processing.
- The fact that this project is a bachelor's thesis comes together with a big drawback, time. A deadline will be present and a lot of data collecting and processing still must be done.
- Sample size plays a crucial role in this research. It is hard to get iEEG recordings from humans, thanks to the Hospital Clinic, we can obtain them with the consent and participation of the patients, but still, the number of measurements is limited.
- Finally, the extent to which findings from the study can be generalized to broader populations may be limited by the specific characteristics of the sample or experimental conditions.

1.4. IDIBAPS and Hospital Clínic

This research will be carried out mainly in three places. All data is collected in the Epilepsy Unit from the Hospital Clinic of Barcelona so that it can be processed at the Institut d'Investigacions Biomèdiques August Pi I Sunyer (IDIBAPS), more specifically in the Compte Lab. This is the place where meetings take place and most of the data processing and analyzing is performed too, although a lot of it will be done independently at home or similar working places too.

2. BACKGROUND

2.1. General concepts

2.1.1. Working memory:

It is a brain function that works as a very short-term memory system, it provides temporary storage and processing of information needed to perform cognitive tasks, such as learning or reasoning. It also plays a role in language comprehension, it holds on to the words in a sentence long in off so that we can give sense to what we are listening to, but after not very long, we will not be able to perfectly recall the words we just heard. Another useful example of an application of working memory is how the brain can maintain continuity in a constantly changing world, the visual system uses recent past inputs to inform perception in the present, harnessing the self-repeating nature of events in the visual environment [4].

2.1.2.Activity-based memory maintenance

When information is retained in the working memory through sustained neural activity of specific brain regions, we talk about activity-based memory maintenance. It often involves continuous firing of neurons responding to external stimuli or other internal cognitive processes, this allows to consciously hold information to be used immediately or in ongoing tasks [5, 6].

2.1.3. Activity-silent memory maintenance

Activity-silent memory maintenance puts forward that transient alterations in synaptic efficacy, rather than continuous spiking activity, support the retention of information in the working memory. In this context, stimulus-induced short-term synaptic plasticity in prefrontal circuits can transiently store mnemonic content when neuronal firing recedes [7]. These synaptic traces usually exhibit a decay time constants on the order of seconds, allowing information to persist across brief delays without requiring persistent neural activity. Studies have shown that, although prefrontal spiking returns to baseline after the stimulus offset, the encoded information remains latent and can be reactivated by proper cues, suggesting that synaptic modifications constitute the basis for this silent storage [8]. Therefore, this activity-silent mechanisms provide a plausible account of how the prefrontal cortex (PFC) sustains working memory representations during inter-trial intervals and contributes to serial biases observed in working memory tasks [9].

2.1.4. Short-term synaptic plasticity

It comprises transient, use-dependent modifications of synaptic strength that take place for hundreds of milliseconds to a few seconds, and are mediated by presynaptic changes in neurotransmitter release probability and postsynaptic receptor dynamics [10]. In the context of WM, it is related to activity-silent mechanisms, whereby information is stored in the altered state of synaptic weights rather than in sustained neuronal firing, remains latent through inter-trial intervals and can be reinstated by nonspecific afferent inputs [11].

2.1.5. Encoding and decoding models

Encoding models characterize how stimuli or cognitive variables give rise to neural responses, whereas decoding models invert this logic, and use neural activity to predict or reconstruct those stimuli or variables. Consequently, encoding analyses are often used to characterize response tuning, and decoding analyses probe the fidelity and temporal dynamics of information available for perceptual or mnemonic processes.

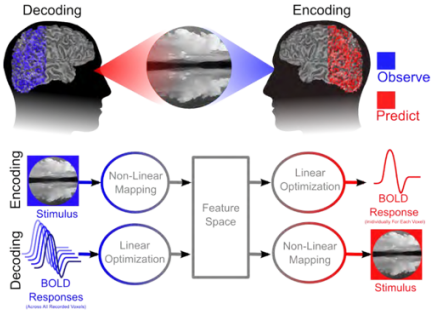

Figure 1. Encoding versus decoding schematic [12].

2.1.6. Univariate and multivariate analyses

Univariate analyses examines each neural feature individually, whether a single electrode's amplitude, power or firing rate, to assess how one signal correlates with experimental variables. Instead, multivariate analyses consider the joint activity across multiple sensors, time points or neurons as a high-dimensional pattern. Multivariate approaches show the advantage of capturing distributed representations and interactions that univariate tests cannot reveal, although univariate analyses allow us to determine significant decoding regions of interest (ROIs).

2.2. State of art

This project starts from the research performed and findings obtained about the WM by IDIBAPS, more specifically by Compte Lab, with Albert Compte as team leader, and aims to expand the knowledge in this field. Therefore, during this section I will dig in into recent discoveries, mostly from Compte Lab, related to WM and serial biases.

2.2.1. Introduction to serial dependency bias in perception

Vision must coordinate two seemingly opposing demands, firstly, the need to detect sudden changes in the environment with high sensitivity, and secondly, maintain a stable representation of visual inputs, which often arrive as noisy and discontinuous inputs, despite the physical world being generally stable. Classical studies have demonstrated how prolonged exposure to a particular visual stimulus property such as orientation may lead to negative aftereffects, thereby enhancing sensitivity but introducing repulsive biases in perception [13]. Fischer and Whitney tested whether perceptual reports are attracted towards stimuli previously experienced seconds earlier, a phenomenon they termed "serial dependence" [14].

In a series of psychophysical experiments, participants observed randomly oriented Gabor patches at suprathreshold contrast, and after several seconds, adjusted a response bar to the perceived orientation. Reported orientations were robustly drawn towards the orientation of previous stimulus, showing an attractive bias of $\pm 8º$, when the difference between successive orientations was close to 28º. It was also seen how the bias persisted, although diminished, for stimuli two and three trials back ($\approx 15s$). Control conditions ruled out contributions from motor repetition, explicit memory, priming or expectation [14].

Fischer and Whitney's finding revealed a previously unrecognized operator in human vision, a spatiotemporal continuous field that attracts perceptual estimates towards recent history mediated by attention and spatial proximity. By integrating past and present inputs, serial dependence may serve as an adaptative mechanism to stabilize perception, while still permitting sensitivity to genuine change. The bias vanishes when successive orientations differ markedly, and its gating attention dissociates it from change blindness arising from inattention [14].

2.2.2. The interplay between serial dependence and working memory

Fritsche, Mostert and de Lange (2017) challenged the Fischer and Whitney view by which serial dependency effects consisted of perceptual biases. They aimed to disentangle the contributions of perceptual and post-perceptual to the biases induced by recent events. To do so, they alternated between two types of tasks, which distinguished between perceptual (a change in how you see the

stimulus) and working memory (a change in how the information used to make a response is store in short term memory) biases. In some trials, observers adjusted a response bar to the remembered orientation, in others, they made a quick decision about which of two options was closer to the previous stimulus or whether both orientations were the same [15].

They demonstrated how attractive biases do not originate at the level of sensory encoding, but instead arises during post-perceptual stages. The magnitude of positive biases incremented as the retention interval lengthened, indicating that working-memory representations drift towards prior decisions over time. This temporal dependence implicated mnemonic dynamics rather than altered perceptual encoding. Conversely, the repulsive perceptual aftereffect was highly spatially specific, thereby linking it to early sensory pathway. It was speculated how these opposite effects could arise from different goals, where perception optimizes change detection, and decision processes integrate information over time to form stable representations, hence, differentiating between perceptual and post-perceptual effects [15].

This dual-mechanism suggests that the nervous system balances sensitivity to new information with the need for representational stability through distinct perceptual and mnemonic processes. By dissociating these contributions Fritsche, Mostert and de Lange lay the groundwork for future investigations in neural circuits and successfully link serial dependence with the working memory [15].

2.2.3. Neural mechanisms of serial dependency bias

Mechanisms of working memory maintenance have long been attributed to persistent spiking activity in recurrent cortical circuits, particularly within the prefrontal cortex (PFC), where sustained firing rates delay periods correlate with mnemonic precision. Although recent proposals argue for an alternative approach based on ‘activity-silent’ substrates, plausibly mediated by short-term synaptic plasticity or intrinsic cellular processes, thus permitting subsequent reactivation of latent activity [11].

Barbosa et al. 2020 defied this belief by proposing how attractor dynamics that control neural spiking interact with the activity-silent mechanisms in the PFC. Researchers combined intracranial recordings in four monkey’s dorsolateral prefrontal cortex, human EEG decoding and transcranial magnetic stimulation to demonstrate that, following a period of undetectable delay-period firing, latent synaptic traces maintain previous-trial information during the inter-trial interval (ITI). This information is reactivated just prior to the presentation of new stimuli and the strength of the reactivation correlates with the magnitude of serial biases in spatial working memory [11].

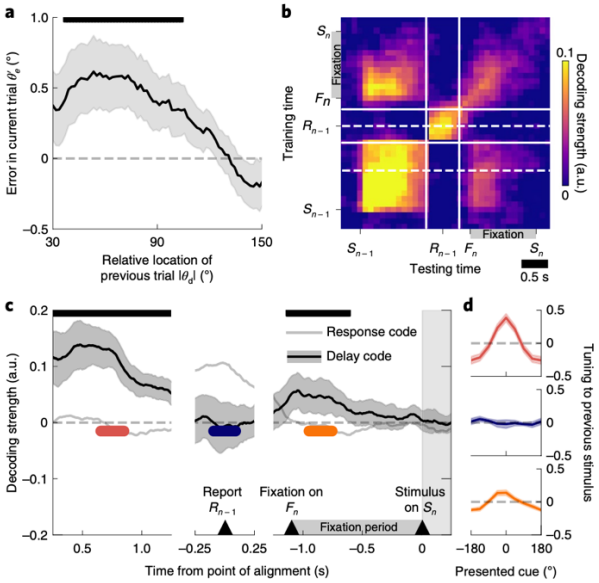

Figure 2. In human EEG, the delay code also reactivates in the fixation period. Where a) is the serial bias representation is human participants, b) is a temporal generalization of previous stimulus from previous trial onset (S_{n-1}) and response (R_{n-1}), to current trial fixation period (F_n) and stimulus onset (S_n), c) shows the decoding of previous stimulus during previous-trial delay (left), response (middle) and current-trial fixation period (right) for decoders trained during previous-trial delay. Finally, d) represents the de-meaned reconstruction of tuning to the previous stimulus at different epochs for the delay decoder, marked in c [11].

Figure 2a shows that human observers exhibit serial bias. Furthermore, *Figure 2b and 2c* prove that a decoder trained on delay-period alpha-band topographies can track the previous trial's stimulus not only during its maintenance and response epochs but also reactivates in the fixation period of the following trial. The tuning curves reconstructions in *Figure 2d* reveal significant selectivity for the previous stimulus during the delay and the subsequent fixation, mirroring the monkey PFC data, while showing no tuning at the time of response, thereby demonstrating that an activity-silent synaptic trace holds the retention and reinstatement of spatial working memory across trials [11]. Interestingly, this reactivation at the time of fixation in the task is absent in patients with anti-NMDAR encephalitis and schizophrenia [16], in line with their reduced attraction serial dependence [17].

The study proposes a bump attractor model with short-term plasticity (STP) to explain these findings. In this model, memory is held as an activity bump during the delay period, imprinted on neural synapses as a latent activity-silent trace during the ITI. This latent bump can be reactivated by nonspecific anticipatory signals, influencing subsequent memory and behavior. Overall, these findings suggest a dynamic interplay for memory storage and serial biases in spatial WM [11], but cannot specifically identify what brain areas are responsible for memory reactivations. This is the question that motivated the investigation of intracranial signals during this task in this TFG.

2.2.4. Clinical manifestations: Reduction of serial dependence in NMDAR encephalitis and schizophrenia

Autoimmune encephalitis (AE) gathers a variety of non-infectious, immune-mediated inflammatory conditions affecting the brain, where anti-N-methyl-D-aspartate receptor (NMDAR) encephalitis makes an appearance as a leading type. This condition is due to the appearance of autoantibodies targeting the NMDAR NR1 subunit [18]. In the other hand, schizophrenia is chronic mental disorder

which impacts nearly 1% of the global population. Evidence suggests that disturbances in excitatory signaling, particularly the hypofunction of the N-methyl-D-aspartate receptor (NMDAR), play a role in the disease's progression. Although both share similar features such as cognitive deficits in working memory and psychosis, the former is distinguished by prominent movement disorders and seizures, and misdiagnosis is common in early stages [17, 19].

Stein et al. 2020 showed how when spatial working memory performance is examined, healthy individuals exhibit and increasing attractive bias towards previously viewed locations, reflecting serial dependence. In contrast, patients with schizophrenia display a repulsive bias away from past stimuli, whereas those recovering from anti-NMDAR encephalitis show an attenuated attraction similar in direction to controls but of markedly reduced magnitude. Across all groups, recall precision diminishes with longer delays, and follow-up testing in encephalitis patients reveals that as clinical symptoms remit, their serial-dependence biases normalize toward control levels [17].

Short-term synaptic plasticity temporarily retains stimulus-specific information during intervals lacking sustained focus, such as inter-trial intervals (ITIs), thereby influencing memory recall in subsequent trials. The underactivity coming from the NMDAR, could potentially decrease STP, which would indeed lead to reduced reliance on past stimuli in memory processes [17].

2.2.5. Preprocessing strategies and the current debate on their impact

Neuroscientists have long believed that removing noisy or artifactual observations from electrophysiological recordings enhances statistical power to find subtle patterns or relationships, however, pure distinction between low-level noise and genuine neural data is often unachievable, therefore forcing us to find a balance between sensitivity and specificity. In particular, although standard techniques readily eliminate well-defined interference, such as 50/60 Hz mains hum, many contaminating spectral and spatial features overlap with true neural activity, leaving researchers without a clear criterion for data cleaning. To address this ambiguity, a recent study applied both statistically-driven, automated pipelines and manual expert reviews to iEEG recordings. They tested both methods using univariate and multivariate methods and found no difference between both, which let them to suggest that to improve further analysis, we should focus on incrementing sample size, rather than data cleaning [20].

Another study by Delorme revealed that high-pass filtering exerts the greatest influence on downstream sensitivity for scalp EEG. To compare filtering cutoffs, artifact-rejection algorithms, referencing schemes and baseline they used a task-relevant metric, which mostly consisted of the number of channels showing significant evoked responses. They demonstrated that employing a high-pass cutoff between 0.1 Hz and 0.75 Hz can increase the number of significant channels by up to 57%, whereas conventional line-noise removal via notch filtering or spectral methods and fully automated ICA-based cleaning yielded no consistent gains and often reduced sensitivity. Among the pipelines used for data processing, EEGLAB, Brainstorm, MNE, Fieldtrip… were tested [21].

In large-scale evaluation of iEEG, neither automated statistical filters nor manual rejection enhanced the power to detect broadband signatures of episodic memory encoding, instead, artifact detection pipelines often sacrificed more trials than any gain in sensitivity, thereby challenging the

assumption that data cleaning inherently improves posterior analysis [20]. Delorme corroborates these results showing how notch filtering, re-referencing schemes, and advanced artifact-rejection algorithms yielded negligible or even detrimental effects, with high-pass cutoff filters being the only beneficial methodology. Together, these findings suggest that expanding sample sizes or within-subject trial counts, rather than investing disproportionate effort in elaborate preprocessing, represents the most effective strategy for bolstering statistical power in electrophysiological studies [21].

3. MARKET ANALYSIS

3.1. Market overview

Brain disorders are a leading and growing cause of disability worldwide and cause death second to cardiovascular diseases. Due to our growing and aging population, the currency of this disorders has increased significantly by a 48% since 1990s. Neurological and neuropsychiatric disorders are responsible for 9 million and 8 million annual deaths, respectively. It has been analyzed that the GNM was worth $612 billion in 2022, with a 73% coming from non-drug therapies, and it is expected to grow up to $721 billion by 2026, returning an aggregate compound annual growth rate of 4.2 percent across segments [22].

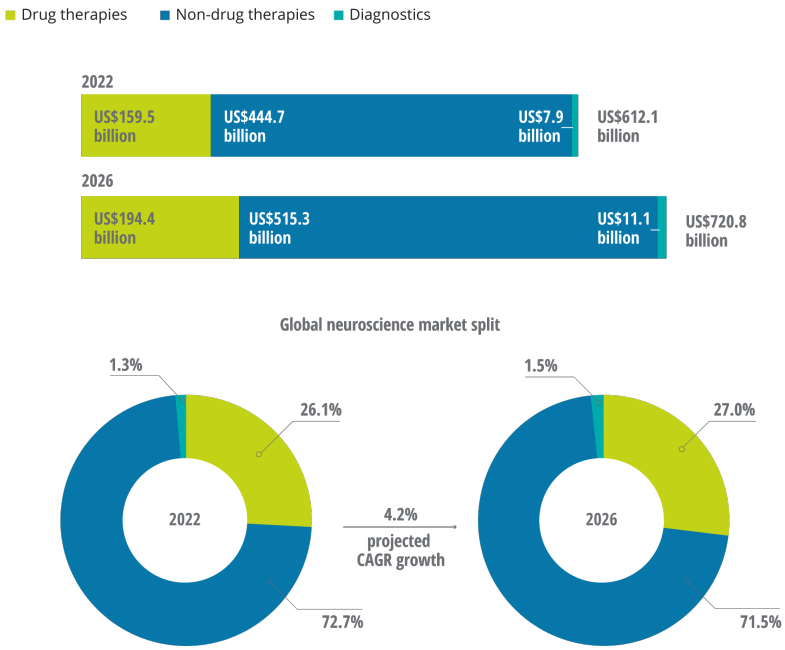

Figure 3. Neuroscience market revenue for drug and non-drug therapeutic techniques and diagnostic tools [17].

3.2. Target market

The main beneficiaries of advances in cognitive-task decoding and preprocessing comparison are healthcare systems, brain-machine interface development companies, and academic and research institutions.

3.2.1. Healthcare professionals and hospitals

Improved insights into cognitive processes allow for more accurate diagnostic tools and therapeutic methods for conditions such as the discussed above in *Section 2.2.4*. Thereby translating into better personalized care and treatment and advanced neurorehabilitation techniques. This said, the research benefits healthcare providers and hospitals addressing complex problems with a much greater precision and efficacy.

3.2.2. Brain-machine interface development

Deciphering how the human brain encodes and manipulates information remains a challenge in neuroscience, yet it is precisely this that motivates the creation of algorithms capable of translating neural activity into actionable commands. Recent advances in intracranial recordings and machine learning decoding have motivated projects as Neuralink and Cognixion to develop brain-machine interfaces aimed at restoring cognitive and motor functions. Within this context, our project's focus is especially pertinent. By refining preprocessing and decoding pipelines that accurately isolate and classify multivariate EEG patterns we contribute to the technological necessities for these types of interfaces which can reincorporate impaired cognitive processes.

3.2.3.Academic and research institutions

Academic and research institutions are the main target audience in the short term for advanced neural data pre-processing and decoding solutions. Universities and dedicated neuroscience research centers focus deeply on state-of-art electrophysiological platforms and software pipelines to broaden the knowledge about the neural mechanisms supporting cognition, publishing in high profile journals and secure competitive grants. The increasing availability of large, open-access intracranial datasets and the need for reproducible, shareable analysis tools have amplified the demand for flexible, transparent preprocessing frameworks that can be adapted to diverse experimental designs. By providing a rigorous comparison of manual, semi-automatic and automatic pre-processing strategies for artifact rejection alongside decoding analyses, our project meets the needs of academic labs seeking both methodological rigor and ease of implementation in collaborative, multi-site studies.

3.3. Market competition

As seen and explained earlier, neuroscience is a growing market with lots of opportunities intriguing many people around the globe, there is no doubt then that everyone will want a piece of it.

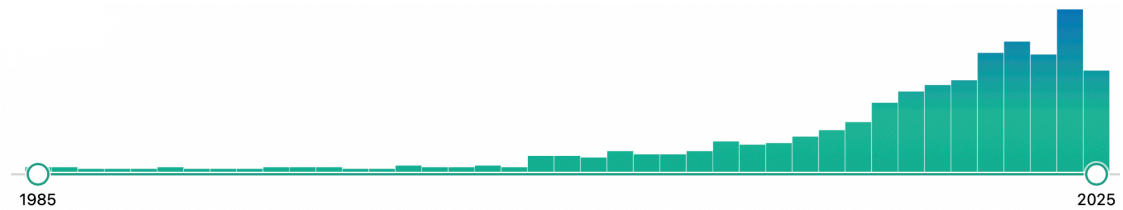

Figure 4. Number of articles written yearly found in Pubmed by using advanced search mechanisms.

It is appreciated in *Figure 4* the exponential growth involving neuroscience. This result was obtained thanks to the following query: *("iEEG" OR "intracranial EEG" OR "electrocorticography" OR "EEG") AND (preprocessing OR "artifact rejection" OR filtering OR referencing) AND (decoding OR*

classification OR "pattern analysis") and a total of 704 results are obtained, with 99 articles published in 2024 and currently 61 in 2025.

4. CONCEPT ENGINEERING

In this section, all methods and steps needed to proceed with the project will be considered and discussed, including other possible options that could have been used. Although, prior to explaining the range of possibilities considered for this project, it is necessary to present an overview of our approach to concept engineering. Initially, raw neurophysiological data undergo preprocessing and artifact removal through three different methods: a fully automated algorithm, a semi-automatic pipeline, and a manual evaluation. Following this systematic cleaning, we subject the processed datasets from each pipeline to both univariate and multivariate analyses, thereby enabling the identification of serial biases and the bump-attractor theory in iEEG, delineation of candidate regions of interest associated with serial biases, and most importantly, a quantitative comparison of cleaning efficacy across pipelines. Finally, as a preliminary result, we built an encoding model using the subject whose data showed the best performance, these preliminary results will serve as a foundational framework for subsequent investigation into neural investigations.

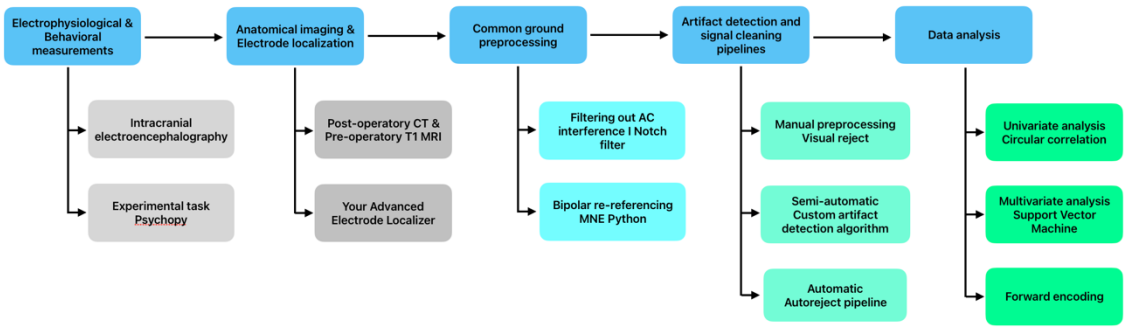

Figure 5. Concept engineering schematic summary.

4.1. Data acquisition

Since the people participating in the research have been hospitalized in the Hospital Clinic of Barcelona to find the area of the brain causing their epileptic seizures, there are not many options to choose how to take the corresponding measurements and brain images. Nevertheless, the methods used provide us with precious information, where in other scenarios, they could not have been carried out and are the driving force behind the motivation of the project. Three types of information are distinguishable among our data. All three will be reviewed in the following subsections, explaining the method used, other possible methods, reasonings and process for data acquisition.

In total, the dataset is composed of 15 new subjects. Due to time constrains, for this study only 5 subjects will be analyzed.

4.1.1. Electrophysiological and behavioral measurements

To take the electrophysiological measurements necessary, only one option was considered, since it is most likely the best and a big motivation behind this research. Thanks to the advances in

technology of the Hospital Clinic, it is one of the few centers in Spain qualified to perform iEEG registers, therefore many patients who suffer from epilepsy and need a more sophisticated diagnosis attend the hospital.

Thanks to the cooperation of the Hospital Clinic and the patients hospitalized, we can take these recordings of electrophysiological activity from inside the brain, offering much more information than regular EEG. Therefore, iEEG is the technique used.

Participants will be playing a small game of 2 sections, 45 minutes each, each one divided in 6 small blocks of 50 trials, while recordings are taken. Each trial commences with a central fixation point displayed in the center of the screen for 1.1 seconds. Followed by this, a circle shows for 0.25 more seconds randomly at any of the 360 degrees angular possible positions. After this stimulus is presented, there is a delay period, also randomly selected between 1 to 3 seconds, during which only the fixation square remained visible. Then, patients are asked to click with the cursor the remembered position of the stimulus. After the response, the cursor goes back to the fixation dot to initiate a new trial (ITI). The error is computed as the angular distance between response and the actual site of the stimulus.

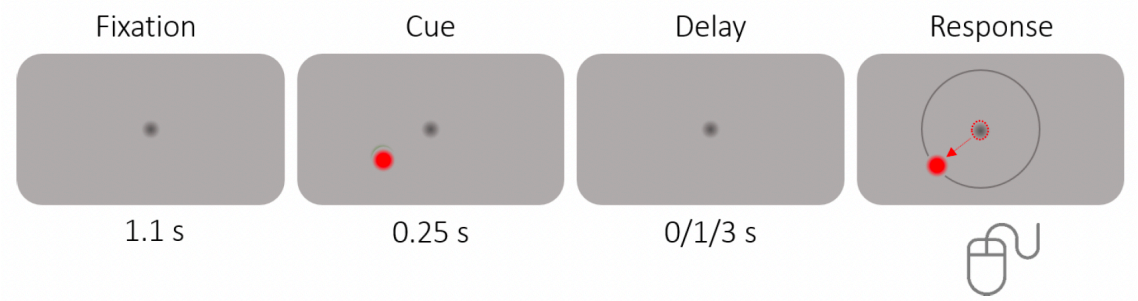

Figure 6. Task schematic representation that participants will be performing while recordings are taken.

The reason behind dividing the experiment in 2 sections is to study statistical learning. During the first block, all stimuli have a uniform probability of appearance among the 360 degrees. Although, in the second section, stimuli have a higher probability of appearance to show in specific places.

During fixation, cue and delay periods participants must be looking all the time at the fixation dot, to ensure that this happens, an eye tracker device is needed. At the budget end, there are webcam-based eye trackers, which offer limited accuracy and speed in tracking eye movements. Moving up the ladder, portable eye trackers come next, although they have been discarded for this study since they are worn in the patient's heads, making hard to combine it together with the implanted electrodes. Following these are screen-mounted eye trackers, employing infrared technology for highly accurate eye movement tracking. Finally, as the option that could potentially be the best, although also the most expensive, there are eye trackers which use retinal photography or corneal mapping.

For the study we ended up choosing the screen-mounted eye trackers, being the most equilibrated option. Although it is important to consider that light differences along the trial or the use of glasses can difficult its use too.

For the design of the experimental game, Psychopy on Python was used. Other platforms that also show themselves as good alternatives are OpenSesame, which can also run on Python, it is a free and open-source with very good capabilities and friendly-user interface. E-Prime on the other hand has an extensive built-in functionality and offers a very strong technical support, although it is less flexible compared to open-sources options and requires licensing fees.

While *Psychopy* offers flexibility, open-source availability, and a large user base, other programs like *OpenSesame* and *E-Prime* provide alternative options with varying levels of user-friendliness, functionality, and cost.

4.1.2. Anatomical imaging

As explained in the previous sections, there is not much room for variability of methods used when acquiring the data. The anatomical images that we obtain are the ones that the doctor considers necessary to offer the best possible diagnosis. That being CT and T1 MRI images.

4.1.2.1. Location of implanted electrodes

Many programs are available for the location of electrodes, in this section they will be briefly discussed, and our selection will be explained.

- FieldTrip toolbox: It is free and open-sourced in MATLAB, very useful when analyzing neuroimaging data, including EEGs. It even also provides tools for source reconstruction and statistical analysis, although it is mostly used to reconstruct 3D models for scalp EEG rather than localizing intracranial electrodes [23].
- iELVis: Which is short for Intracranial Electrode Visualization is a software toolbox consisting of MATLAB and Bash scripts for intracranial localization and visualization. It is well tailored for iEEG depth and grid electrodes and integrates FSL and Freesurfer. Although it is command-line oriented with no dedicated GUI [24].
- Brainstorm: It posed a big chance to being the selected option due to its fully interactive GUI and popularity. Brainstorm is also integrated with Freesurfer and returns useful coordinates as MNE and RAS, although despite its fully interactive GUI, its steep learning curve made us go for the last and next option [25].
- YAEL: It stands for Your Advanced Electrode Localizer. This is the option we went for. Its main use is for iEEG and by installing YAEL, two popular tools for co-registering the MRI and CT datasets are automatically installed, Advanced Normalization Tools (ANTs) and Nifty Reg. YAEL is also an open-source option which offers a friendly-user GUI interface, very easy to use, with a lot of potential which directly assigns MNE and RAS coordinates to the localized electrodes, together with labels according to the brain region the shafts have been implanted [26].

4.2. Data pre-processing

As introduced in the beginning of this work, a current debate in computational neuroscience is: *How much benefit do we gain by preprocessing our neural data before running decoding analyses?* To

answer this, we will implement and compare a set of preprocessing pipelines with different characteristics. Each pipeline's output will then be used in identical decoding frameworks; by systematically evaluating each method we aim to provide concrete, data-proven guidance on when and how to preprocess neural recordings.

4.2.1. Common groundwork

All our preprocessing pipelines share a set of common steps, filtering out AC interference and re-referencing of electrodes. The following sections will expand on these two topics and the reasoning behind their solutions.

4.2.1.1. Filtering out AC interference

Electrophysiological measurements are routinely affected by narrowband interference at the AC-mains frequency, 50Hz in Europe, and its harmonics. If not handled properly, it can distort significantly both time-domain waveforms and spectral estimates. To suppress this artifact, we utilized a second-order digital notch filter centered at 50Hz, 100Hz, 150Hz and 200Hz. Notch filtering in this configuration offers significant advantages. Firstly, its narrow stop-band design minimizes distortion of neighboring frequencies, and secondly, the use of standard IIR topology ensures computational efficiency. However, fixed frequency notch filters can underperform if the mains interference drifts outside the nominal center frequency, which usually happens if a power system has unstable loads [27].

Several alternatives that could help fixing this drifting issue include broadband band-stop filters, which achieve the suppression of the entire 48-52Hz, at the cost of attenuating physiologically relevant signal components near the margins [28]. Inverted band pass filters con be used to construct a comb filter, they reject the power-line frequency and its harmonics in one step by summing delayed versions of the signal, placing zeros on the unit circle at 50Hz, 100Hz, 150Hz and 200Hz [29]. While they have proven to be highly effective for our situation, notch filter is better integrated into the MNE-Python library, hence being our final decision.

4.2.1.2. Bipolar re-referencing

Bipolar re-referencing involves computing the difference between two adjacent electrodes, the anode and the cathode, thereby creating a new bipolar virtual electrode where shared noise between neighboring contacts is attenuated. Because intracranial channels often exhibit volume-conduction and common-mode artifacts, the subtraction enhances the detection of real local fluctuations and improves the specificity of downstream spectral or time-domain analysis.

Although popular toolboxes as EEGLAB offer re-referencing via its *pop_reref* function, where pairs of channels can be defined interactively or scripted, we chose to implement all referencing steps with the MNE-Python environment. To do so we developed a function that prepares data into a set of consecutive anode-cathode electrode contacts to be fed to MNE's *set_bipolar_reference* function, which generates the new virtual channels while preserving the montage [30, 31].

Beyond bipolar derivations, alternative referencing methods deserve to be mentioned. The common-average reference (CAR) subtracts the mean across all intracranial shafts individually to each electrode contact, thereby offering a global baseline. Building upon this idea, the adaptative

common-average reference (ACAR) integrates CAR with an adaptive noise-cancelling (ANC) filter in a convergent feedback loop, such that the CAR output serves as the reference for the ANC stage, which in turn refines the CAR estimate. This method has proven to outstand CAR, and even on some occasions, show better results than independent component analysis [32]. More recently, the Reference Electrode Standardization Technique (REST) has been proposed to approximate a neutral reference at infinity, reducing bias introduced by any single physical reference [33]. During this work we will primarily focus on bipolar derivation due to their ease of interpretation in intracranial scenarios and support within MNE-Python, ensuring that the entire pipeline remains harmonized under a single open-source platform.

4.2.2. Manual pre-processing

In our first preprocessing strategy we follow the traditional “by-hand” approach to neural data cleaning. This method starts with a preliminary global inspection of the recording, during which we usually identify and drop channels exhibiting excessive noise or artifacts. Once all channels are revised the common groundwork is applied and we segment the remaining data into epochs around events of interest.

At this stage, there are two alternative approaches:

1. Epoch-by-epoch visual inspection: The procedure consists of examining each epoch and rejecting trials that show residual noise or movement artifacts. While this method maximizes the trade-off between sensitivity and specificity if performed correctly, it is extremely time-consuming for large datasets and strongly subjective. Therefore, due to the limited amount of time available in this work and the little experience reading iEEGs, this method was not chosen.
2. Hybrid Visual Reject Toolkit: To mitigate the labor burden and human bias of epoch review, we developed the Visual Reject Toolkit. This set of functions integrates three components, a flexible quantitative metric calculator (for variance, peak-to-peak amplitude, kurtosis…), an interactive GUI and auxiliary visualizations for outlier detection.

By choosing option two, rather than spending hours of scanning every single epoch, researchers review only those segments that exceed certain thresholds, this hybrid approach introduces objective statistics into the manual method to guide human decisions.

4.2.3. Automatic and semi-automatic methods

Automatic and semi-automatic artifact-rejection routines identify and exclude contaminated trials by applying different statistical thresholding criteria depending on the algorithm. Thresholds can be learned by the model if fully automatic, and are usually inferred directly from the data, often via cross-validation or robust estimation techniques, thus ensuring objective data-driven decisions that frequently surpasses manual judgments in consistency and sensitivity. In contrast, semi-automatic pipelines combine algorithmic candidate selection with user-defined thresholds, affording precise control over the balance between artifact removal and signal preservation.

EEGLAB again poses great advantages, being a popular choice for most people since the early 2000s (Delorme & Makeig, 2004). Its modular plugin architecture allows integration of advanced

preprocessing algorithms, including those for automated channel rejection, rejection of noisy epochs and Independent Component Analysis (ICA) decomposition. Although as previously mentioned, MNE-Python methods are prioritized. In that sense, Autoreject appears, a fully automated method which employs cross-validation to optimize sensor specific peak-to-peak thresholds [34]. While Autoreject has proven outstanding results in scalp EEG, for which it was designed, its performance in iEEG is still under debate, although with the proper considerations it might turn out to perform decently.

Despite the fact that we did not adopt it in our pipelines, the PREP framework offers a compelling example of how Random Sample Consensus (RANSAC) can be leveraged for robust channel-quality assessment. Bigdely-Shamlo et al. 2015 proposes and implementation methodology, over 50 iterations, the algorithm samples 25 % of electrodes as provisional inliers, reconstructs the full multichannel signal via spherical-spline interpolation, and computes the point-wise median. Channels whose correlation with this median falls below 0.75 for more than 40 % of the recording are flagged as bad and interpolated, yielding a common-average reference resilient to spatially correlated noise.

Staresina et al. (2015) describes a semi-automatic pipeline for artifact rejection based on three scores: amplitude, gradient and frequency envelope. It applies morphological operations to dilate artifact segments, remove small runs of clean data in between marked clusters, a zero-phase FIR filter, and finally the main body of the pipeline, where each score is calculated and measured against a common threshold for artifact detection.

For our study, we chose to adapt Staresina's approach with a few modifications which will be explained in *Section 5* alongside with Autoreject's fully automated algorithm. By preprocessing the dataset with a manual, a semi-automatic, and an automatic method, we achieve a comprehensive evaluation of each pipeline's efficacy in balancing artifact suppression and preservation of genuine neural signals, thereby informing optimal choices for subsequent decoding analyses.

4.3. Data analysis

4.3.1. Univariate and multivariate decoding

In our univariate analysis, we sought to assess the relationship between single neural features and the experimental variable of interest, thereby quantifying the decoding significance of each channel. To this end, we used circular-linear correlation, which are well studied to quantify associations between angular data and a continuous predictor. To establish a statistical threshold that accounts for the non-Gaussian nature of data, we implemented a non-parametric permutation test in which labels were randomly reassigned to neural data. By repeating this procedure for multiple permutations, we can obtain the null distribution of circular correlation coefficients at each location for a determined frequency band.

Despite the fact that we chose to go for circular correlation, alternative univariate strategies could have been employed. Fields and Kuperberg et al. 2020 explain the use of mass univariate statistics for Event-Related Potential (ERP) data analysis to enhance flexibility and power. Their approach calculates separate statistical tests at multiple time points and electrodes individually, followed by a multiple comparisons correction to control the Type 1 error, falsely rejecting the null hypothesis

when it is actually true. The method uses specialized corrections like Falsely Discovery Rate (FDR) and resampling procedures to estimate the null distribution. One of the main advantages of this method is a greater flexibility in detecting effects across space and time and better control over false positives, but they can complicate precise temporal and spatial interpretation and may underestimate effect duration. And as explained earlier, one of the objectives of univariate analysis is to locate spatially significant decoding channels, this being the reason this method did not fit our goals as much as circular correlation [35].

In parallel, our multivariate analyses were designed to use joint information contained across multiple channels to predict the experimental variables. We adopted a Support Vector Machine (SVM) classifier from the multichannel neural patterns at different time windows of interest by computing the Power Spectral Density (PSD) at different frequency ranges. This classifier again used permutation tests to accumulate the null distribution of errors over numerous repetitions. We chose to perform this analysis using PSD features since it allowed us to summarize oscillatory activity over a given window, thus reducing the dimensionality and noise associated with raw time-resolved signals. Additionally, by performing time-frequency analysis, we can gain more information on how different brain waves relate to our analysis.

We preferred SVM over Linear Discriminant Analysis (LDA) because SVM does not assume Gaussian distributions or equal covariance across classes, instead, it finds the maximum-margin hyperplane that best separates conditions, which makes it more robust to high-dimensional PSD features and outliers.

4.3.2. Forward encoding model analysis

Forward encoding models (or inverted encoding models) represent a widely adopted strategy for modeling how stimulus features give rise to neural responses. They work by creating a set of hypothetical neural channels, each one tuned to a specific value along a continuous stimulus dimension, which in our case consists of a particular remembered stimulus orientation. By measuring how strongly each channel is activated during a task, we can obtain tuning curves, a profile showing the relative response magnitude of all channels across the stimulus space continuously in time. These curves can give us information as how sharply or diffusely this population is tuned to a particular feature [36].

In contrast to standard classifiers, which simply categorize neural patterns into discrete labels, forward encoding provides a continuous reconstruction. In multivariate classifiers, we can obtain information of whether a particular feature is being decoded or not if the returned output beats chance level, but this information does not tell us how the representation is distributed or biased [36].

Moreover, Alexis Perez's publicly available toolbox facilitates the fitting of forward encoding models, thereby providing validated routines to construct basis functions and estimating weight matrices without extensive coding. Consequently, since forward encoding delivers a more refined depiction of neural representations, rather than a simple correct or incorrect label, it was the option chosen for this final preliminary analysis.

5. DETAILED ENGINEERING

Previously, in section 4 *Concept Engineering,* the rationale behind the chosen steps and alternative approaches was discussed. In this section, *Detailed Engineering,* each of those steps will be thoroughly analyzed, including the underlying logic and implementation details.

5.1. Initial data preparation and structuring

As a first step in preparing the data for publication, the raw iEEG recordings together with their associated behavioral data (metadata) were organized and standardized. This involved defining subject and session identification, concatenating the relevant EDF files, and loading the correspondent electrode coordinate files. Electrode labels were cleaned and matched to the recording channels in the raw EDF files to ensure consistency in the analysis and proper posterior localization. Only relevant recording channels were kept, together with the TRIG channel, which contains the events occurring during the experiment, needed to extract the epochs.

The channels dropped consist of generic non-informative channels (C1 to C256), which could correspond to ground or diagnostic outputs from the recording device, or unused amplifier channels. It is common for clinical systems to list all possible channels the system can handle, even if only a subset of them is connected to electrodes. Therefore, they may contain flat, noisy, or empty data which could mess with our analysis.

Additionally, physiological monitoring data not relevant to our neural data study was also dropped, including channels as oxygen saturation (OSAT), pulse rate (PR), plethysmograph (Pleth) and electrocardiogram leads (EKGL/EKGR).

Subsequently, experimental events were extracted from the trigger channel and added to the raw data as annotations. Channel types were defined according to their corresponding function (SEEG and simulation), and the dataset was converted to the BIDS (Brain Imaging Data Structure) format to facilitate standardization and reproducibility using the MNE-BIDS framework. Anatomical images (defaced ACPC-aligned T1 weighted MRI and CT scans) were also included to support future localization and coregistration.

5.2. Data cleaning and preprocessing pipeline

Along this section, the three chosen methods for data preprocessing (simple manual cleaning with visual reject, Autoreject, and custom artifact detection algorithm) will be explained in detail. All alternatives share common groundwork, that being a first visual inspection to drop clearly bad channels, the application of a notch filter, bipolar re-referencing, extracting epochs and adding metadata.

5.2.1. Common groundwork

5.2.1.1. Notch filter

A fundamental aspect of the data cleaning pipeline consists of the application of a notch filter to remove power line interference, a common source of narrowband noise in electrophysiological recordings. A notch filter is a type of band stop filter made from a combination of both high-pass and low-pass filters, they are extremely effective at removing interfering signals at specific frequencies. They are also referred as band-rejection filters. In this case, it was applied at 50 Hz

and its harmonics (100 Hz, 150 Hz, 200 Hz), which correspond to the frequency of AC mains electricity in the recording environment.

Power line noise can distort spectral estimates and obscure neural signals. In contrary to a common band-stop filter, a notch filter is specially tuned to only suppress the undesired frequency components, while preserving nearby ones, thereby minimizing the attenuation of neural activity. From an engineering point of view, this filter allows us to increase the signal-to-noise (SNR) ratio, without introducing significant phase distortion or degrading temporal resolution [37].

This operation follows a second-order transfer function, commonly represented as:

$$H(s) = H_0 \frac{s^2 + w_z^2}{s^2 + \frac{w_0}{Q} s + w_0^2}$$

Equation 1. Notch filter second-order transfer function (Analog Devices, 2006).

Where $w_0=2\pi f_0$ is the angular notch frequency and Q is the quality factor defining the bandwidth of the notch. This form is specially well suited for biomedical engineering applications since it provides for targeted attenuation while preserving the phase and magnitude of neighboring neural frequencies. There are three types of notch filters determined by the relationship between zero frequency (w_z) and the pole frequency (w_0). In our case, we used a standard notch filter, where $w_z = w_0$, and a sharp attenuation at the frequency is created. Alternatively, there are two more cases, a lowpass notch ($w_z > w_0$) and high-pass notch ($w_z < w_0$), in those cases attenuation favors lower or higher frequencies, behaving as an elliptical low-pass or high-pass filter respectively. Although these last two options did not suit the application we were looking for [38].

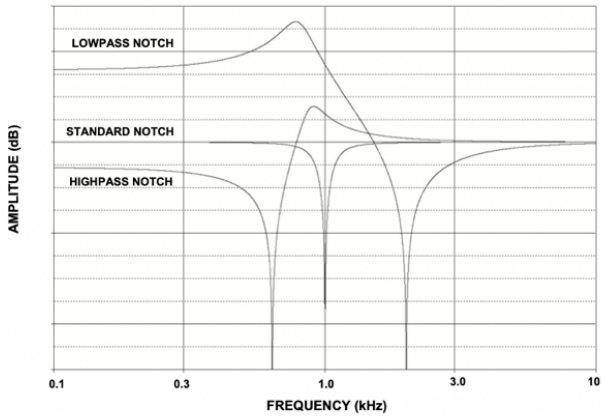

Figure 7. Standard, Low-pass and High-pass Notches (Analog Devices, 2006).

Harmonics of 50 Hz were filtered out too since non-linear loads and devices on the power system caused harmonic distortion in the current and voltage. An ideal linear system receives a sine wave at 50 Hz and gives a sine wave back. Although, when a non-linear system receives a sine wave, it can generate distorted waveforms that break down into a sum of sine waves at multiples of the original frequency, harmonics. Therefore, a slightly non-linear amplifier, converter or medical device can distort the original signal and create multiples of it [39]. These extra frequencies can overlap with real high-frequency neural signals such as high-gamma.

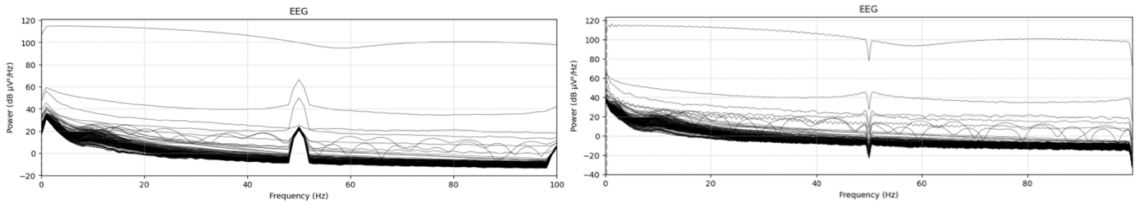

Figure 8. Power Spectral Density (PSD) before notch filter in the left and after notch filter in the right.

Afterwards, raw data was resampled from 2048 Hz to 500 Hz for storage and code optimization purposes, while keeping all essential frequency ranges of neural activity. According to Nyquist theorem, 500 Hz allows for time-frequency analysis up to 250 Hz, which includes all neural data frequency ranges we were aiming to study.

5.2.1.1. Bipolar re-referencing

In intracranial EEG (iEEG) recordings signals are often acquired in a referential montage, this means that all electrode contacts are recorded against a common reference. This reference is usually a surface electrode, a distant intracranial contact or even sometimes a dedicated wire. If the reference electrode picks up physiological noise, electrical interference or activity from distant neural sources, it will be embedded in all channels. The brain signal at the reference location might not be zero, which may contaminate the true measurements and hide local activity introducing common-mode signals. To mitigate these effects a bipolar re-referencing function was designed and applied.

Bipolar referencing consists of computing the voltage different between two adjacent contacts on the same electrode shaft, hence transforming the dataset from a referential montage to a bipolar montage. Mathematically, for two neighboring contacts C_i and C_{i+1}, a new virtual bipolar signal (V_{bip}) is defined as:

$$V_{bip}(t) = V_{C_i}(t) - V_{C_{i+1}}(t)$$

Equation 2. Virtual signal after bipolar referencing.

Therefore, if any common noise between both contacts was present it will be eliminated improving spatial resolution and emphasizing local neural activity changes between closely spaced contacts. It effectively increases the SNR for local field potentials and improves the detectability of high frequency artifacts as seizure patterns.

To implement this transformation computationally, electrode contacts were grouped based on the electrode label prefix, which is commonly shared between each contact of the same shaft, and sorted numerically based on their suffix, thus ensuring anatomical order. Once adjacent contacts were paired, the MNE-Python *set_bipolar_reference()* function was used to generate these new virtual bipolar signals.

5.2.1.2. Epoch extraction and metadata addition

At this stage of the code, preprocessed brain recordings are carved into small sized segments of 6 seconds surrounding each task event of interest. These raw data segments are called epochs, and are extracted from the fixation point event, 1.5 seconds before and 4.5 seconds after, just about

enough time to answer our questions and see if previous trial information can be decoded in the current trial and cover the longest possible 3 second delay. In parallel, we assemble all the trial-by-trial behavioral measures, such as stimulus parameters, participant's responses, delay period, and the relationship of each trial to its neighbors, into a single table, which is then added to each epoch's metadata.

By slicing the data in events and enriching it with its own metadata, simple raw sensor measurements now turn into a highly structured dataset where brain signals and behavioral activity can be analyzed and decoded.

Up to this step, all iEEG cleaning methods shared a common set of steps. In the following sections, each method will be explained individually.

5.2.2. Visual reject

The Visual Reject toolkit consists of a collection of custom functions built around three complementary concepts: a flexible metric calculator, an interactive GUI for artifact or outlier marking both in channels and trials, and auxiliary visualization for both Autoreject and MNE plotting. All together, these functions combine a basic solution for cleaning iEEG epochs by combining both quantitative outlier detection and subjective human decision-making.

5.2.2.1. Metric calculation

The metric calculation routine reduces each epoch's full time series into scores per trial and channel, thereby allowing us to rank or threshold them by how "noisy" or "outlying" they appear. We begin with a 3D array matrix of shape *(nº of epochs, nº of channels, nº of time points per epoch).* Let:

$$D_{n,c,t,}\ 0 \le n < N, 0 \le c < C, 0 \le t < T$$

Denote the voltage at time *t* in channel *c* and epoch *n.* Since Visual Reject may also be used in other preprocessing pipeline, where possible NaNs might have been introduced after artifact cleaning, the code firsts scans *D* for any NaN entries. If any are found, it will flag the user, but it will not crash subsequent calculations. Different scores are calculated for data visualization, including variance and standard deviation:

$$\sigma_{c,n}^2 = \frac{1}{T'}\sum_{t=1}^{T}(D_{n,c,t} - \mu_{n,c})^2$$

Equation 3. Variance of the signal in channel c and epoch n, computed over the non-NaN samples.

Where $\mu_{n,c} = \frac{1}{T'}\sum_t D_{n,c,t}$ is the mean over the non-NaN samples and T' is the count of valid non-NaN time points. In the code this calculation is incorporated via *np.nanvar(…, axis=1).* Standard deviation is also available and is calculated in NumPy Python via *np.nanstd(…, axis = 1).* Both indicate how widely the signal varies around its mean. If the desired, the inverse of the variance can be shown too, where a small $\varepsilon = 10^{-308}$ protects the code against the rare case of a division by zero due to a completely flat epoch:

$$M_{c,n} = \frac{1}{\sigma_{c,n}^2 + \varepsilon},$$

Equation 4. Inverse-variance metric with a small constant ε to prevent division by zero.

For robustness against rare high-amplitude spikes, we also support median absolute deviation (MAD):

$$MAD_{c,n} = median(|D_{n,c,t} - median_t(D_{n,c,t})|)$$

Equation 5. Mean absolute deviation mathematical formula for a channel c and epoch n.

And kurtosis:

$$k_{c,n} = \frac{\mathbb{E}|(D-\mu)^4|}{\sigma^4} - 3$$

Equation 6. Excess kurtosis of the signal in channel c and epoch n.

In Python, these measures are implemented thanks to the *Scipy Stats* package, via the *median_abs_deviation()* and *kurtosis()* functions respectively.

In practical terms, variance delivers a computationally efficient estimate of signal power, its simplicity, stability and fast convergence on iEEG windows make it our go-to metric in preprocessing. Kurtosis may be a good alternative in cases where more data is available, and researchers are willing to try more computationally expensive methods.

Simpler measures are also available, as peak-to-peak voltage, or maximum and minimum. Although they might not reflect as good as variance potential outliers by possibly confusing them with clean data.

5.2.2.2. Interactive artifact-rejection interface

Users get full access control over which trials and channels to exclude via a single function that spawns an interactive window combining quantitative summaries with click-and-drag selection. The function requires an *MNE.epochs* object, once received, it extracts all relevant data channels into a three-dimensional array *(epochs x channels x times)* and computes the chosen metric score. This interactive interface consists of 4 subplots; an initial metric matrix displayed as a heatmap, with channels as the y-axis and epochs as the x-axis, two accompanying scatterplots show the "badness" score per channel and per trial (averaged over non-rejected channels or trials respectively), and finally a spectrum panel displaying the average power-spectral density (PSD) of all currently "good" data. As we reject trials and channels genuine oscillatory peaks of physiological bands as alpha and beta remain stable, while artifactual frequencies diminish, thereby demonstrating effective cleaning choices. When the user closes the window, the function returns two sorted lists, rejected trials and channels.

5.2.2.3. Spectrum-based sanity check

As said above, the spectrum panel is an indicator of the cleaning quality, since artifact rejection here is driven by the user and not an automated threshold, it serves as a real-time sanity check guiding manual selections. It is computed using the Welch's method, which in contrary to a Full

Fast Fourier Transform (FFT), it returns a smoother spectral decomposition which is easier to interpret. The Full FFT performs the Fourier Transform over the entire duration of the signal, thereby it is more sensitive to noise, since artifacts will affect the whole signal. Instead, Welch's method computes the Fourier Transform over small time-windows of tapered data, therefore smoothing noise, since one artifact will not affect the entire signal, but only a small number of time-windows [40].

To apply Welch's method, the continuous time-series is broken down into *M* overlapping chunks of length *L*. In our code, *L = min(T,256)* samples, with a 50% overlapping between successive windows. Each chunk of data is multiplied by a Hamming window *w[n]*:

$$w[n] = 0.54 - 0.46\cos\left(\frac{2\pi n}{L-1}\right), \quad 0 \le n < L$$

Equation 7. Mathematical definition of the Hamming window of length L.

By tapering the edges, we suppress spectral leakage smoothly bringing the edges of each segment to zero. This way, after applying the discrete Fourier Transform, no high-frequency components will be introduced from abrupt jumps at the boundaries. Then, for each window segment $x_i[n] = w[n] \cdot segment_i[n]$, the DFT is computed:

$$X_i[k] = \sum_{n=0}^{L-1} x_i[n] e^{-j2\pi kn/L},$$

Equation 8. Discrete Fourier transform of the i^{th} windowed segment.

And form the raw periodogram:

$$P_i[k] = \frac{1}{UL}|X_i[k]|^2$$

Equation 9. Normalized periodogram of the i^{th} windowed segment at frequency bin k.

Where the normalizing constant $U = \frac{1}{L}\sum_{n=0}^{L-1} w^2[n]$ corrects the window's energy loss. Finally, the PSD estimate at each frequency bin *k* is the arithmetic mean of the M periodograms:

$$\hat{S}[k] = \frac{1}{M}\sum_{i=1}^{M} P_i[k].$$

Equation 10. Power spectral density estimate via Welch's method.

Averaging reduces the variance estimate, hence returning a smoothed curve where true oscillatory components stand out clearly. One main drawback Welch's method faces is a reduced spectral precision when compared against "Full" FFT, this disadvantage resides in the fact that when the continuous time signal is divided into many time-windows, we reduce the number of time points for each DFT, thereby reducing resolution [41].

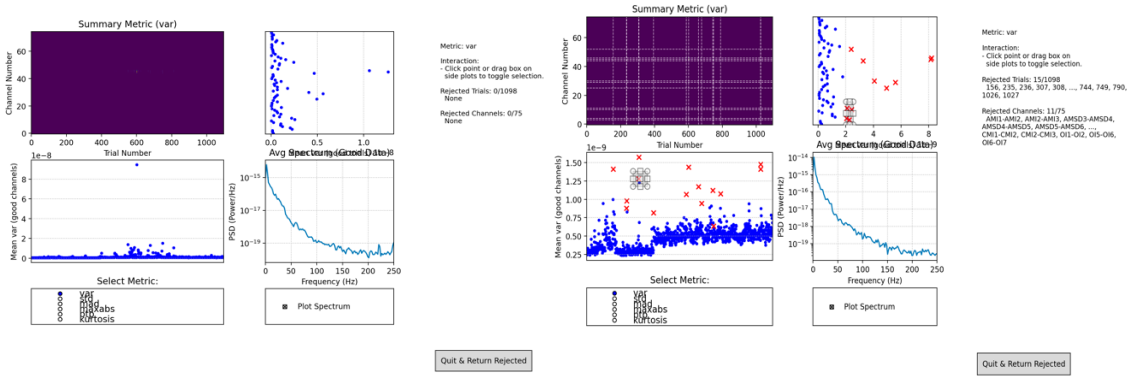

Figure 9. Visual Rejection interactive screen. From left to right a) Before bad channel and trial selection b) After bad channel and trial selection.

In *Figure 9*, the heatmap in the top-left represents the current channel and trial selection. In the top-right and bottom-left corners we can find the channel and trial "badness" scores respectively. Finally, in the bottom-right side of the screen, the spectral panel is shown, it can be seen, how after cleaning, the two high-frequency peaks most likely representing artifacts are gone.

5.2.3. Custom artifact detection algorithm

Our custom artifact detection pipeline brings together three complementary stages; spectral filtering, outlier marking, and morphological cleanup, into a single Python implementation inspired by Staresina et al. (2015). Prior to feature extraction, data is optionally segmented and run through a zero-phase FIR Filter, allowing low-pass, high-pass, band-pass or notch responses depending on cutoff parameters. This first step ensures that the gradient and high frequency envelope metrics are computed on spectrally tailored data without edge artifact or phase distortion [42]. Next, rather than relying on mean and standard deviation, we normalize each channel's signal by its median and median-absolute-deviation (MAD), this way the detector becomes inherently resistant to outliers and therefore more robust. Artifacts are detected through a median/MAD-based "z-scoring" threshold of amplitude, slope, and high-frequency envelope.

Once artifacts are flagged, we now adapt two more concepts explained by the paper, segment expansion and gap-filling. EEG artifacts might corrupt nearby clean data, to ensure this does not happen, a segment expansion function called *Padding* is created, this padding routine dilates each contiguous artifact cluster by a fixed number of samples on both sides. Afterward, small clean data gaps between larger artifacts are also flagged as noise, thus preventing small holes of data from slipping through [42].

5.2.3.1. Padding

We begin with a binary artifact mask sequence defined as $d = (d_1, d_2, \dots, d_T), d_T \in \{0,1\}$. Where $d_t = 1$ means that the corresponding sample *t* has been marked as an artifact and 0 clean data. Our objective is to expand each contiguous run of ones by a fixed integer padding radius $\mathcal{p} > 0$ and $\mathcal{p} \in \mathbb{N}_0$, which indicates how many samples before and after the artifact run do we want to mark.

$$d_t = \begin{cases} 1, sample\ t\ is\ flagged\ s\ an\ artifact, \\ 0, ample\ t\ is\ clean. \end{cases}$$

Equation 11. Precise definition of the binary artifact mask.

The first step in the padding function is to define a set of all originally marked artifact sample indices as $S = \{t: d_t = 1\}$, mathematically, S is decomposed into its connected components, in other words, runs of consecutive integers C_m. Formally, there is a unique partition:

$$S = \bigcup_{m=1}^{M} C_m$$

Equation 12. Decomposition of the artifact set into M maximal contiguous clusters.

Each cluster is a maximal interval run of integers in S, which can be denoted as $C_m = \{a_m, a_{m+1}, \dots, b_m\}$, where $a_m = minC_m$ and $b_m = maxC_m$. By construction, each run C_m lives entirely inside the set of artifact-marked samples S, such that each $d_t = 1$ for $t \in C_m$. These runs are maximal in the sense that you cannot extend them one step further without leaving S. For each run the algorithm creates two intervals for both left and right padding. Left padding is described by:

$$L_m = \{a_m - p, \dots, a_m - 1\} \cap \{1, \dots, T\},$$

Equation 13. Mathematical definition of the left-padding interval of radius p, clipped to the valid sample range.

This is the block of *p* samples immediately before the run, but clipped so that it never goes below the first sample, similarly, the right padding interval is defined as:

$$R_m = \{b_m + 1, \dots, b_m + p\} \cap \{1, \dots, T\}.$$

Equation 14. Mathematical definition of the right-padding interval of radius p, clipped to the valid sample range.

So that the padded runs can be assembled from the overall padded artifact set:

$$S_{pad} = \cup_{m=1}^{M} (C_m \cup L_m \cup R_m).$$

Equation 15. Expanded artifact set after dilation by padding.

Finally, the padded binary mask is produced following the definition below:

$$\tilde{d}_t = \begin{cases} 1, t \in S_{pad}, \\ 0, otherwise. \end{cases}$$

Equation 16. Padded binary mask ($\tilde{d}_t$) returned by the padding routine.

5.2.3.2. Remove small segments

Intuitively, this routine follows a similar logic to the padding function. We start again with a binary mask where $d_t = 1$ marks an artifact and $d_t = 0$ clean data. A clean sample set is defined as $C = \{t : d_t = 0\}$, just as the reasoning above, *C* can be decomposed into *K* maximal contiguous runs of connected components:

$$C = \bigcup_{k=1}^{K} E_k, \quad E_k = \{c_k, c_{k+1}, \dots, d_k\},$$

Equation 17. Decomposition of a clean sample set into K maximal contiguous clusters.

Where $c_k = minE_k$, $d_k = maxE_k$, and $d_t = 0$ for $t \in E_k$. Each run's length is defined as:

$$\ell_k = d_k - c_k + 1$$

Equation 18. Length of the k[th] clean segment.

Given a user-specified minimum segment length *L>0,* we identify all too short clean runs as $\mathcal{K}_{small} = \{k : \ell_k < L\}$. We then convert each one of the marked segments into artifacts by defining the filled artifact set:

$$\mathcal{S}_{fill} = \bigcup_{K \in \mathcal{K}_{small}} E_k$$

Equation 19. Set of all samples in undersized clean gaps.

And assemble the post-processed artifact set $\mathcal{S}_{new} = \{t : d_t = 1\} \cup \mathcal{S}_{fill}$. Ultimately, the output mask is:

$$\tilde{d}_t = \begin{cases} 1, t \in \mathcal{S}_{new}, \\ 0, otherwise. \end{cases}$$

Equation 20. Final binary mask after removal of small gaps.

5.2.3.3. EEG Filter

Before any artifact metrics are computed, each channel's raw trace is run through a zero-phase FIR filter configurable by the user. For it, two Python functions are used *firwin* to create the FIR filter coefficients and *filtfilt* to avoid phase distortion.

Initially, parameters are validated, and the filter order is selected. Both low-cutoff and high-cutoff frequencies are allowed as function parameters. In the beginning of the routine, 4 important parameters are defined, the Nyquist frequency, a filter order scaling factor (set to 3) to ensure the filter is neither too short or too large, a minimum filter order (set to 15) and a transition band width controller (set to $\delta = 0.15$). Next, we validate the cutoff frequencies so that $0 \leq f_{lo} \leq f_{hi} \leq f_{Nyq}$. If no explicit filter order is given, it is computed as:

$$M = \max\left(minimum\ filter\ order, scaling\ factor \times \frac{f_s}{f_{cut}}\right)$$

Equation 21. Filter order M chosen as the greater of a minimum order.

FIR filter, especially when using *filtfilt, which* applies the filter forward and backward, need a buffer of data around the edges to prevent artifacts from originating. To avoid them, *filtfilt* first reflects data by padding the data at both ends by a length called *padlen* which can be defined as:

$$padlen = 3 \times (filter\ length - 1)$$

Equation 22. Length of the edge-padding buffer required by zero-phase FIR filtering.

Therefore, we divide each channel's time sample trace into segments of length *L*, requiring that $L \geq 3M$. The filter taps are built via *firwin* using a simplified version of the Hamming window. Depending on whether both or only one cutoff frequency are specified the desired amplitude response vector is designed. For example, for a band-pass filter where both cutoffs are given by the user we define a vector $[0, 0, 1, 1, 0, 0]$ at frequencies $[0, f_{lo}(1-\delta), f_{lo}, f_{hi}, f_{hi}(1+\delta), f_{Nyq})$. The main function incorporates one more parameter which the user can select, *revfilt,* if set as *True*, we invert the response to get a notch filter. Each filter is convolved forwards and then backwards with the FIR taps, canceling all phase delay.

5.2.3.4. Artifact detection

The artifact detection function is the core of our pipeline, here is where artifacts are detected, and the other three functions are integrated all together. It implements three sequential stages: robust feature extraction, adaptative thresholding and morphological cleanup. Unlike traditional approaches that rely on a single mean/STD threshold (as in Staresina et al., 2015) or peak-to-peak limits (as in Autoreject). This algorithm computes three independent z-score metrics per channel; amplitude, slope, and high-frequency envelope, each normalized by the channel's median and MAD. Because median/MAD estimators are far less influenced by extreme outliers than mean/STD, the detector will remain stable even when very large artifacts are present. For a more in depth understanding, let us denote a single channel's time series by $x[n], n = 1, \dots, N$, and define three separate z-score measurements:

$$z_{amp}[n] = \frac{x[n] - median(x)}{MAD(x)},$$

$$z_{grad}[n] = \frac{\Delta x[n] - median(\Delta x)}{MAD(\Delta x)},$$

$$z_{env}[n] = \frac{e[n] - median(e)}{MAD(e)}.$$

Equation 23. From top to bottom: a) Amplitude based z-score of the raw signal $x[n]$ normalized by its median and MAD, b) Slope-based z-score where $\Delta x[n]$ denotes the first derivative of $x[n]$, also normalized by median and MAD, c) Median/MAD normalized high-frequency envelope.

In *Equation 23 c)* $e[n] = \left|\mathcal{H}\{x_{hp}\}[n]\right|$ is the analytic signal envelope of the Hilbert transform of the 240Hz high-pass filtered original signal. Each sample *n* is the initially flagged if any of:

$$z_{amp}[n] > \tau_{amp}, \quad z_{grad}[n] > \tau_{grad}, \quad z_{env}[n] > \tau_{env}$$

Equation 24. Initial artifact flagging condition.

Where $\tau_{amp}, \tau_{grad}, \tau_{env}$ are user defined thresholds in MAD units. Subsequent steps prune spuriously short decisions, unless they contain a giant spike controlled by an overshoot factor also determined by the user, dilate the remaining clusters by $\mathcal{p}$ samples on each side (padding), and clean any short gaps shorter than a minimum duration. After these steps the final artifact mask is applied to the data.

As a special note, the artifact detection algorithms return the original *MNE* dataset as a *NumPy* array, hence, another function to convert it back to its original format is implemented after the data cleaning.

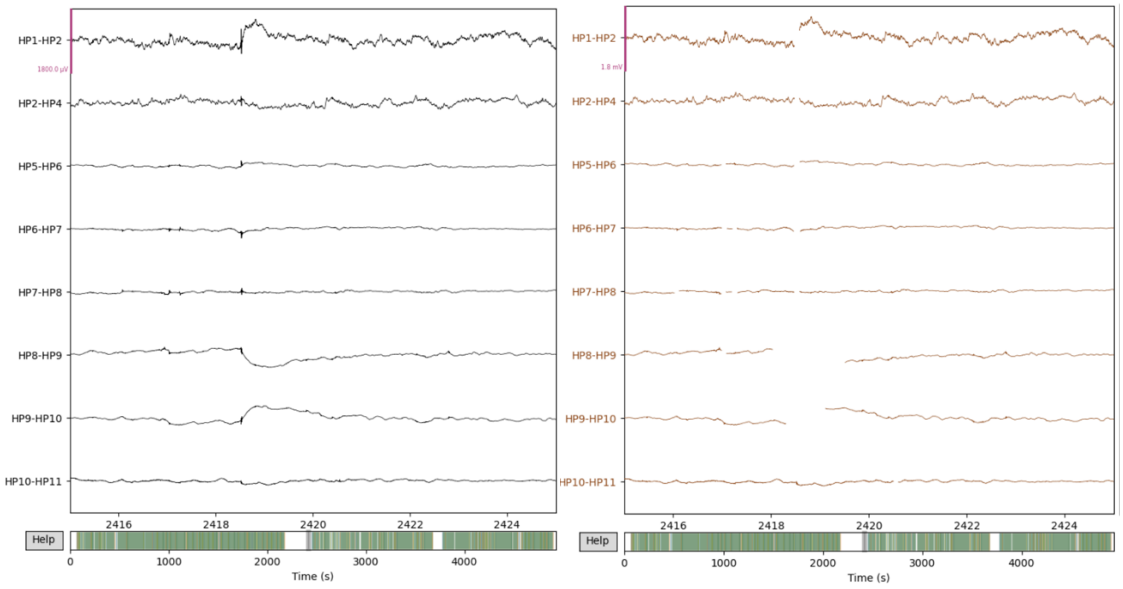

Figure 10. Artifact detection output for a time for a 10ms time window and 1.8mV scale. Starting from the left a) Original iEEG signal b) Processed iEEG signal.

Figure 10 clearly demonstrates the dual efficacy of our tuned artifact detector. In the middle virtual bipolar channels, it is appreciable how subtle low-level drifts that often evade simple thresholding are blanked out and removed from the data. *HP1-HP2, HP7-HP8* and *HP9-HP10* show bigger-sized artifacts, which are also successfully detected. By combining robust median/MAD normalization with independent amplitude, slope, and envelope thresholds, the algorithm is capable of adapting to both extremes: small-sized blips no longer accumulate over time, and major spikes no longer contaminate the analysis.

5.2.3.5. Trial rejection

During the application of the artifact mask to the original uncleaned signal, the marked regions are converted into NaNs. For further analysis those NaNs must be eliminated. Unfortunately, due to the large number of channels per subject, it is highly probable that for each epoch, there is at least one NaN present in one of the channels, hence, if we limit ourselves to just dropping all trials with NaNs, we will lose almost all data.

In an effort to prevent this, one more step is added to the pipeline, trial rejection. The first step of trial rejection is applying Visual Reject explained in *Section 5.2.2,* this collection of functions offers a versatile approach that fits in diverse pipeline to ensure a proper cleaning of borderline before any hard trial exclusion decisions are made.

Subsequently, the relative amount of NaNs per channel is computed. By first excluding channels whose NaN rate exceeds a predefined threshold and then removing only those epochs that still contain NaNs, we minimize the total number of trials discarded. This procedure involves a delicate

trade-off: sacrificing a subset of channels to preserve a larger number of valid epochs, rather than vice versa.

5.2.4. Autoreject

Traditional EEG cleaning is often based in peak-to-peak amplitude, applied either globally to all sensors or thresholding per channel. This process is time-consuming and prone to experimenter bias. Autoreject automates such tedious procedure by using K-fold cross-validation to automatically learn optimal rejection cutoffs directly from data. For each fold, candidate thresholds minimizing the error are calculated. This process can be applied either to the entire sensor-by-time matrix or to each channel independently. Each trial is marked as "bad" by any channel whose peak-to-peak exceeds its learned cutoff. Trials with too many bad channels are discarded, while those with only a few sensors flagged get interpolated from their neighbors. This interpolation might maximize data retention in scalp EEG, but as explained in section 4 *Concept Engineering,* Autoreject is not fully suited for our iEEG case, meaning that it might not work as it should [43].

5.2.4.1. Threshold learning

To explain it in detail, let our data matrix be $X \in \mathbb{R}^{N \cdot P}$, where N is the number of trials and P is the number of features. For a global threshold $P = Q \times T$ (all *Q* sensors over *T* time points), whereas if threshold is computed channel by channel $P = T$. To simplify the notation, trials are denoted as $X_i = (X_{i1}, X_{i2}, \dots, X_{iP})$. *Where* its across-trial mean is defined as $\bar{X}$ *a*nd its median is $\tilde{X}$. Finally, each trial's peak-to-peak amplitude is measured by:

$$ptp(X_i) = \max(X_i) - \min(X_i)$$

Equation 25. Peak-to-peak amplitude for trial i.

To learn a global cutoff threshold, a K-fold cross-validation is carried out. In each *K* fold, *N* trials are divided into train and validation, peak-to-peak amplitudes for all trials *X* in the training set are computed and stored as $A = \{ptp(X_i) \mid i \in train_k\}$, and finally a subset of "good" trials G_l is defined for those under a candidate threshold $\tau_l \in \mathbb{R}$ as $G_l = \{i \in train_k \mid ptp(X_i) < \tau_l\}$. Once this is determined, the error metric for one CV fold for a particular threshold is computed through the RMSE as:

$$e_{kl} = \left\| \bar{X}_{G_l} - \tilde{X}_{val_k} \right\|_{Fro}$$

Equation 26. Fold-wise error: Forbenius norm between mean of good training trials and median of validation trials.

$\bar{X}_{G_l}$ is the mean of good training trials and $\tilde{X}_{val_k}$ the median of trial in the validation fold, using the median makes the algorithm more robust to outliers $\|\cdot\|_{Fro}$ is the Frobenius norm:

$$\|M\|_{Fro} = \sqrt{\sum_{i,j} M_{i,j}^2}$$

Equation 27. Definition of the Forbenius norm.

CV will find the optimal threshold that does not eliminate or keep too many trials while having the smallest error. The threshold with the minimum mean error is selected as the global threshold:

$$\tau_\star = \tau_{l_\star} \; with \; l_\star = argmin_l \frac{1}{K} \sum_{k=1}^{K} e_{kl}$$

Equation 28. Optimal global threshold minimizing mean CV error.

5.2.4.2. Consensus voting

A single global cutoff often misses channel-specific noise patterns, so instead we learn one optimal threshold $\tau_\star^q$ per sensor *q*, remember that as explained in the beginning, now *P* = *T*. Each sensor then votes a trial as bad if its $ptp > \tau_\star^q$, at the end, any trial with at least a user-defined number of bad sensors is rejected [43].

Cross-validation assumes each sensor has at least some clean trials to learn from, if all trials a bad, it will not be able to establish a baseline. To rescue such channels, data is augmented by creating one "clean" copy of each trial per sensor, interpolating that time-series sensor from its neighbors. Hence, we obtain an augmented matrix, with *2N* rows, where half of them represent raw trials and the other half are the interpolated "cleaned" ones, this new matrix can be defined as $X^a \in \mathbb{R}^{2N \cdot T}$. Just as a quick reminder, this method is designed for scalp EEG, we are doing iEEG, this interpolation technique would be "ideal" if done within each shaft of electrode contacts, and not globally for all shafts. The algorithm then finds for each sensor *j* its optimal peak-to-peak cutoff τ_j^*. Henceforward, sensor *j* believes that *trial i is bad* if that trial's amplitude on sensor *j* exceeds τ_j^* [43].

An indicator matrix $C \in \{0,1\}^{N \cdot Q}$ whose entries $C_{i,j}$ is formed according to the rule:

$$C_{i,j} = \begin{cases} 0, if \; ptp(X_{i,j}) \leq \tau_j^* \\ 1, if \; ptp(X_{i,j}) > \tau_j^* \end{cases}$$

Equation 29. Indicator of whether a sensor j in trial i exceeds its learned cutoff.

That is, we take a consensus among the sensors and mark a trial as bad only if the consensus is high enough. Good trials G are given by $\mathcal{G} = \left\{ i \mid \sum_{j=1}^{Q} C_{i,j} < k \right\}$, in other words: "keep trial *i* if fewer than *k* sensors flagged it as bad". Rather than choosing k as an absolute count, it's often more robust to set it as a fraction of all sensors k/Q [43].

5.2.4.3. Interpolation rescue

After consensus rejection, trials with only a few rejection votes are rescued by interpolating to a maximum of ρ sensors per trial. If a trial has $\leq \rho$ bad sensors, all will be interpolated. Instead, if it has > ρ, but still $\leq k$, so that the trial itslef was not rejected), only the ρ worst sensors ranked based on peak-to-peak amplitude will be interpolated. With this, a score is set, $s_{i,j}$, which is -∞ if the sensor is good and equal to the peak-to-peak amplitude if the sensor is bad:

$$s_{i,j} = \begin{cases} -\infty, if \; C_{i,j} = 0 \\ ptp(X_{i,j}), if \; C_{i,j} = 1 \end{cases}$$

Equation 30. Ranking score per sensor: infinite penalty if clean, else its peak-to-peak.

This leads us to the following rule for interpolating a sensor:

$$X_{i,j} = \begin{cases} interp(X_{i,j}), if\ (0 < \sum_{j'=1}^{Q} C_{i,j'} \leq \rho)\ and\ (C_{i,j} = 1) \\ interp(X_{i,j}), if\ (\rho < \sum_{j'=1}^{Q} C_{i,j'} \leq k)\ and\ (s_{i,j} > s_{i(N-\rho)}) \\ X_{i,j}, otherwise \end{cases}$$

Equation 31. Final Autoreject per-sensor output.

Denote $b_i = \sum_{j'=1}^{Q} C_{i,j'}$, the number of bad sensors in a trial. The optimal values for the parameters $k_\star$ and $\rho_\star$ are estimated using grid search for the same error metric seen earlier in *Equation 26*.

Autoreject results in a fully automated algorithm requiring no manual intervention, particularly useful for large-scale experiments. It also implies that the analysis pipeline is free from experimenter's bias while rejecting trials.

5.2.4.4. Application to our dataset

In implementing this function to our intracranial data, we decided to take two decisions which ultimately will affect the algorithms performance. These considerations were chosen to preserve data integrity and size. Firstly, we disabled per-trial interpolation, as previously mentioned, unlike scalp EEG, where electrode layout is standardized and interpolation might perform well, our shaft-based contacts have variable locations. Moreover, we preferred to avoid introducing synthetic data in an already limited dataset.

Secondly, we set the consensus threshold to $^{k}/_{Q} = 0.3$, in an effort to find a balance between aggressive cleaning and maximal trial retention. At this level around an 80% of trials per subject were maintained. Each function returns a cleaned data array and two interactive RejectLog figures, where dropped and marked trials are highlighted, thus allowing for visual inspection if desired [44].

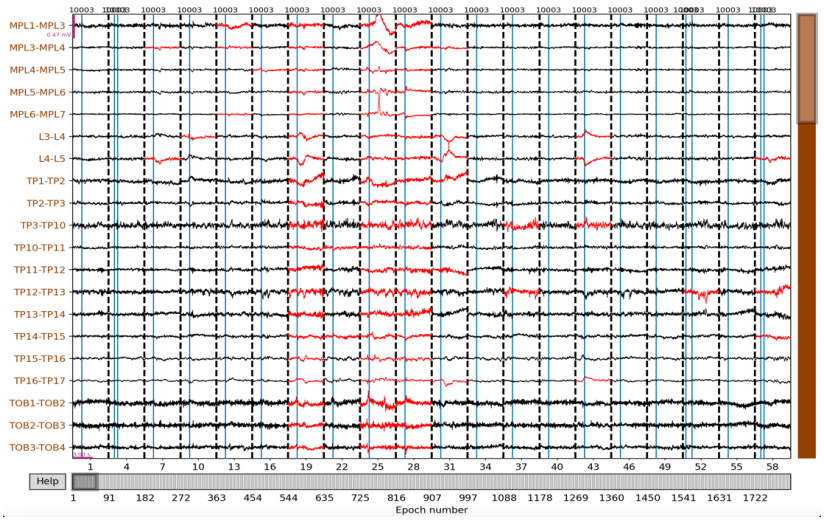

Figure 11. RejectLog visualization for the bipolar virtual channels after Autoreject.

The first flagged epoch in channel L3-L4 exhibits only small, ambiguous deflections, so slight that a human rater would most likely classify it as clean but having fewer than 30% "bad" votes across channels, it is not discarded. Likewise, the final flagged trial of the same channel represents a clear artifact, although it also fails to meet the consensus threshold, and it is retained. This illustrates how consensus balances sensitivity and data preservation.

As illustrated in *Figure 11,* Autoreject seems to continue to perform robustly even with iEEG data after disabling interpolation. It shows to be highly sensitive to low-level artifacts, which occasionally leads to the false identification of clean trials. However, because we employ a consensus threshold, isolated false positives are not automatically discarded, conversely, genuine artifacts that fail to reach the voting threshold will also remain in the dataset.

5.3. Data analysis

5.3.1. Univariate circular correlation

The quantification of the relationship between neural signals and circular behavioral variables needs for special methods that respect the circular nature of the data. In this study univariate circular correlation is used to assess channel-by-channel whether frequency power in intracranial recordings covaries systematically with stimulus orientation. Behind this procedure there are three main steps: firstly, the mathematical formulation of linear circular correlation between neural features and an angular variable, secondly, the estimation of spectral power via the multi-taper method and its normalization to isolate the high-frequency band, and lastly the construction of an empirical null distribution through permutation testing to evaluate statistical significance. Below, each of these three key steps is explained in higher detail:

5.3.1.1. Mathematical foundations of linear-circular correlation

The code implements a linear-circular correlation that relies on separate Pearson correlations with the sine and cosine projections of the angular variable. Let us denote $\alpha = [\alpha_1, \alpha_2, \dots, \alpha_N]^T$ the vector of stimulus orientations for *N* trials, and by $X = N\ x\ P$ a matrix where each column is a linear predictor *P*. The first step is to project each orientation onto its orthogonal components: $u_i = \sin(\alpha_i)$ and $v_i = cos(\alpha_i)$. Then for a given neural feature vector X_p of length N, the Pearson correlation coefficients $r_{x,s,p} = corr(X_p, u)$ and $r_{x,c,p} = corr(X_p, v)$ are computed alongside the scalar $r_{c,s} = corr(v, u)$. Through these three variables we can obtain the squared linear-circular correlation following the equation 8.5.3 (p.187) of Jammalamadaka and SenGupta (2001):

$$R_p^2 = \frac{r_{x,c,p}^2 + r_{x,s,p}^2 - 2 r_{x,c,p} r_{x,s,p} r_{c,s}}{1 - r_{c,s}^2},$$

Equation 32. Squared linear-circular correlation formula.

Because this formula may return a negative value if the arrangement of signs in the numerator suggests an inverted association, the code then uses the signed-square-root convention by computing:

$$R_{signed} = sign(r_{x,s})\, sign(r_{x,c})\, R, \quad R^2 = \sqrt{(R_{signed})^2}.$$

Equation 33. Signed-square-root convention.

Finally, under the null hypothesis of no association the p-value is computed by showing that $NR_{2,p}$ follows a chi-square distribution with two degrees of freedom:

$$p_p = 1 - F_{x_2^2}(NR_{2,p}),$$

Equation 34. Nominal p-value formula.

Where $F_{x_2^2}(\cdot)$ is the cumulative distribution function of X^2 with two degrees of freedom.

5.3.1.2. Extraction and normalization of PSD

The extraction and normalization of the PSD was achieved by using the multi-taper method explained in Chapter 7 of Percival, D. B., and B. J. Walden (1993). *Spectral Analysis for Physical Applications: Multitaper and Conventional Univariate Techniques.* Specifically, for each trial *i* and channel *j,* the raw time series $x_{i,j}(t)$ is multiplied by a series of discrete tapers $h_p(t)$ using the Fourier Transform:

$$X_{i,j,p}(f) = \sum_{n=1}^{T} h_p(n) x_{i,j}(n)^{-2\pi i f n / f_s}, \quad p = 1, \dots K,$$

Equation 35. Tapered Fourier Transform.

And PSD:

$$\hat{S}_{i,j}(f) = \frac{1}{K} \sum_{p=1}^{K} \left| x_{i,j,p}(f) \right|^2,$$

Equation 36. Multi-taper PSD estimate.

Then, to normalize the $\hat{S}_{i,j}(f)$ power $P_{i,j}$, over a target frequency band [f_{low},f_{high}], it is divided by a total broader power $P_{i,j}^{tot}$, additionally, to stabilize ratios a small constant $\varepsilon = 10^{-10}$ was added:

$$y_{i,j} = \log_{10}\left(\frac{P_{i,j} + \varepsilon}{P_{i,j}^{tot} + \varepsilon}\right),$$

Equation 37. PSD normalization for a specific frequency band.

5.3.1.3. Permutation-based construction of the null distribution

Because trial-by-trial covariations between neural data and stimulus angular orientation could be a product of coincidence, it is necessary to assess significance against an empirical null distribution. Let $y_j = [y_{1,j}, \dots, y_{N,j}]^2$ denote the vector of normalized PSD for channel *j*, and let $\theta = [\theta_1, \dots, \theta_N]^T$ be the original sequence of stimulus orientations. The true circular correlation for channel *j* is computed as $r_{j,true} = circ\_corr(y_j, \theta)$. Then, to generate the null distribution for channel *j*, we construct *M* random permutations of $\{\theta(m): m = 1, \dots, M\}$ by applying random shuffles to θ. For each permuted angle vector $\theta(m)$, one computes $r_j(m) = circ\_corr(y_j, \theta(m))$. Because the analysis uses squared correlations, the code stores $R_{j,true}^2$ and $\{R_j^2(m)\}$, to then calculate a one-sided p-value for each channel *j* as:

$$p_j = \frac{1}{M}\sum_{m=1}^{M} 1[\, R_j^2(m) \geq R_{j,true}^2 \,].$$

Equation 38. Null distribution and p-value computation.

Where 1 is the indicator function. Conceptually, if only a small fraction of permuted R^2 values exceed the observed R^2 the channel is statistically significant.

5.3.1.4. Anatomical localization of significant channels

To properly capture the dynamics of frequency bands, the analysis is partitioned into four temporal windows (pre-fixation, fixation, cue and delay), for each subject and time window, each epoch is cropped to isolate the periods of interest, then the resulting subset of data undergoes the process explained above. The frequency band studied goes from 2 Hz to 12 Hz, this being the previously studied frequency band of interest by Compte Lab.

Usually for most studies, a p-value under 0.05 is considered significant, although for ours we chose a stricter threshold of 0.001 to avoid false positives and maximize significance. Once these channels are found, electrode metadata from the previous localization in RAVE containing *FreeSurfer* labels is merged, so that each channel is associated with an anatomical region. It is important to note that white matter areas were previously removed from the dataset. Regions of Interest (ROIs) are plotted through the *aparc.a2009s+aseg* atlas offered by *FreeSurfer* and a count of significant channels per region is tabulated to identify hotspots.

5.3.1.5. Univariate analysis results

This univariate circular correlation is applied to each one of the three preprocessing methods, where the one detecting higher number of significant ROIs would prove to be better for decoding. To turn this comparison into a fair game, the number of channels per method is firstly reduced to only the channels that the three methods have in common.

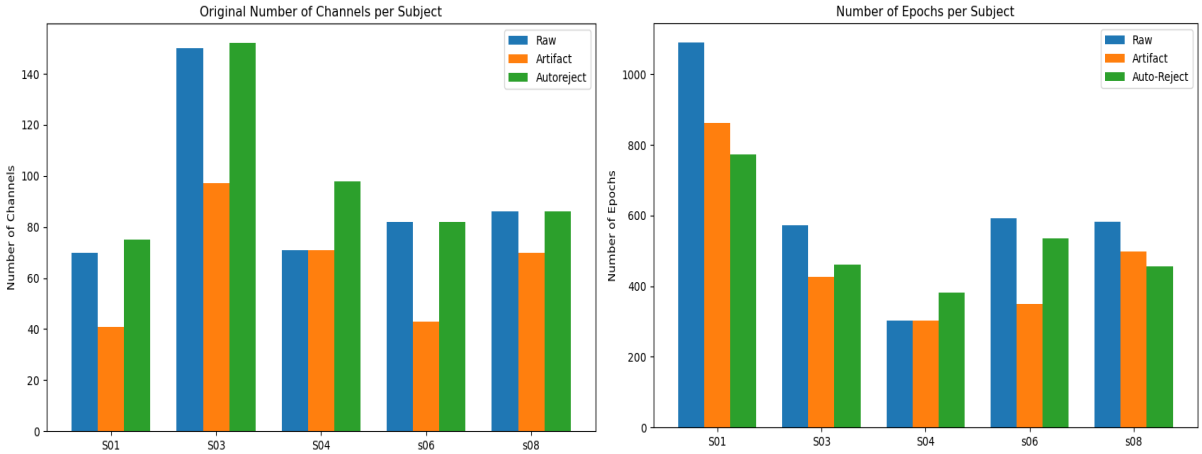

Figure 12. Total number of channels and epochs per method before equilibration.

The table below shows the total number of channels (Ch) per region of interest after reducing the total number of channels only to the ones all methods have in common.

ROI	Ch	ROI	Ch	ROI	Ch
G_precentral (L)	8	G_temp_sup-Lateral (L)	2	G_and_S_cingul-Ant (L)	1
S_intrapariet_and_P_trans (L)	7	G_precentral (R)	2	G_and_S_cingul-Mid-Ant (L)	1
G_pariet_inf-Supramar (L)	5	G_front_sup (R)	2	G_and_S_paracentral (L)	1
G_temporal_middle (R)	5	S_oc-temp_med_and_Lingual (L)	2	G_and_S_subcentral (L)	1
S_precentral-sup-part (R)	5	Lat_Fis-post (L)	2	G_cingul-Post-ventral (L)	1
S_postcentral (L)	5	S_circular_insula_sup (L)	2	G_front_inf-Triangul (L)	1
S_central (L)	4	G_occipital_middle (R)	2	G_temp_sup-G_T_transv (L)	1
G_and_S_cingul-Mid-Post (R)	4	Left-Amygdala	1	G_and_S_cingul-Mid-Ant (R)	1
S_oc_middle_and_Lunatus (R)	3	G_front_sup (L)	1	S_interm_prim-Jensen (L)	1
S_temporal_sup (R)	3	S_oc-temp_lat (L)	1	S_cingul-Marginalis (L)	1
G_parietal_sup (L)	3	S_circular_insula_inf (L)	1	S_front_inf (L)	1
G_precuneus (L)	3	S_front_sup (L)	1	S_calcarine (L)	1
G_temp_sup-Plan_tempo (L)	3	S_temporal_inf (L)	1	G_front_inf-Orbital (R)	1
S_calcarine (R)	3	G_oc-temp_med-Lingual (R)	1	Pole_occipital (R)	1
S_postcentral (R)	3	Lat_Fis-post (R)	1	S_oc-temp_lat (R)	1
S_front_sup (R)	3	S_cingul-Marginalis (R)	1		

Table 1. 47 ROIs, 105 total channels. L=Left hemisphere, R=Right hemisphere. ROIs names simplified (ctx_lh/rh prefixes removed).

Additionally, since this work also aims to study serial dependencies, the univariate circular correlation will be applied both to current stimulus angles, and to previous trial orientations, this

way we cannot only see which brain regions are working on the current stimulus, but also whether there are ROIs working in the previous one, and if so, which ones.

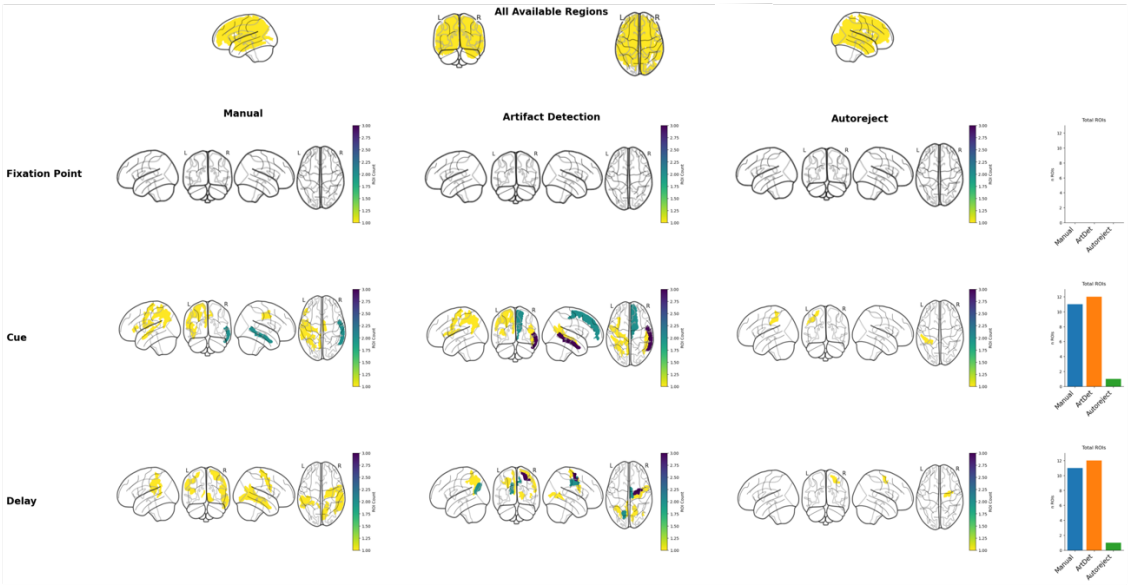

Figure 13. Significant ROIs for univariate circular correlation decoding for the current stimulus.

In *Figure 13,* decoding performance for each method is assessed by examining the presence of significant ROIs during each of the time windows. During the fixation period no ROIs surpass the significance threshold, indicating an absence of decodable activity as expected. The accompanying histograms in the right panel illustrate quantitively the efficacy of each method: the artifact detection approach finds the highest number of significant ROIs, with manually cleaned data to a close second. In contrast, the Autoreject pipeline consistently yields fewer ROIs in every temporal window, suggesting that its automated rejection criteria may not be optimally tuned for iEEG recordings.

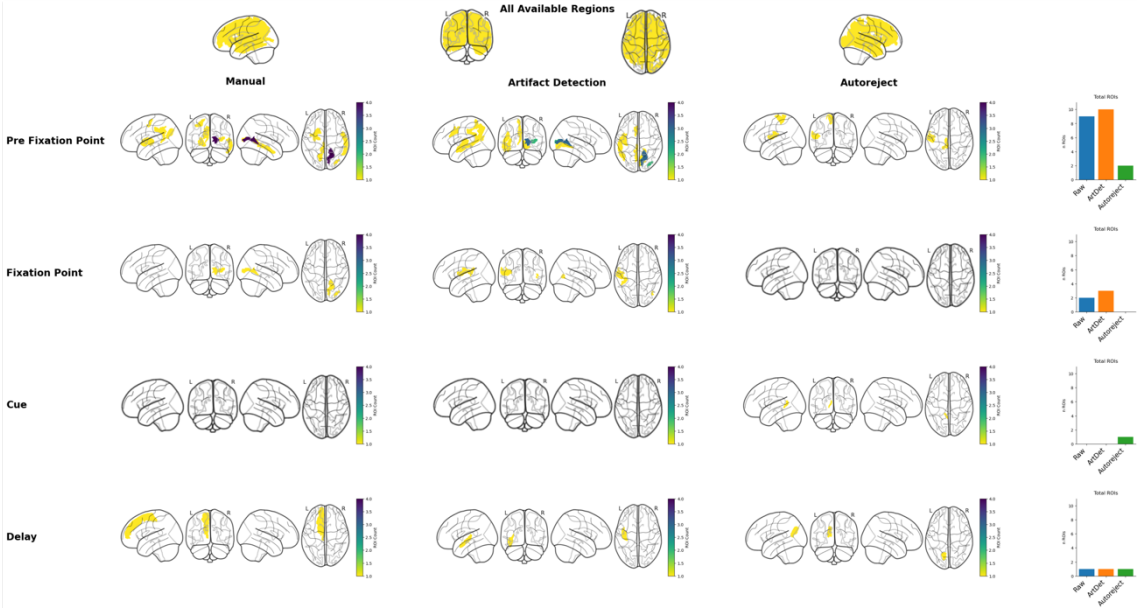

Figure 14. Significant ROIs for univariate circular correlation decoding for the previous stimulus.

Figure 14 depicts the spatial distribution of significant ROIs when decoding the orientation of the previous stimulus, including a pre-fixation interval to highlight baseline activity. Across all time windows the Autoreject method continues to underperform in comparison to the rest. Importantly, during the fixation period manual cleaning identifies two ROIs (the right calcarine sulcus and the right middle occipital-lunatus sulcus), and artifact detection uncovers three ROIs (the left subcentral gyrus and sulcus, the right anterior occipital sulcus, and the left lateral posterior fissure). In contrast, no decoding is present during the cue time window, and one different ROI per method is found in the delay period, which might represent false positive due to the different location of each one. This slight activation in the fixation period when decoding for past trial's orientations follows the logic proposed by the bump-attractor model explained in *Section 2.2.3.*

With respect to the decoding of current stimulus in *Figure 13,* the two most common significant ROIs among all methods and time windows are the right middle temporal gyrus and the right superior frontal gyrus. These anatomical results must be interpreted considering the implantation bias explained during *Section 1.3,* electrodes were placed according to clinical necessity rather than uniform sampling, so regions that fail to appear as often as others may lack coverage.

Although artifact detection shows slightly higher decoding results than manual cleaning, the improvement is minimal, and when applied across all global channels it does not produce a clear global benefit, many channels and epochs are discarded to remove artifacts, which at the end limits the possible results if more brain regions are covered. Artifact removal might pose a significant advantage with respect to manual cleaning when analyses focus on a small subset of channels, since with fewer channels, the chance that any single epoch contains an artifact is reduced, so more clean data is retained despite NaN detection, resulting in a better trade-off between signal quality and data retention.

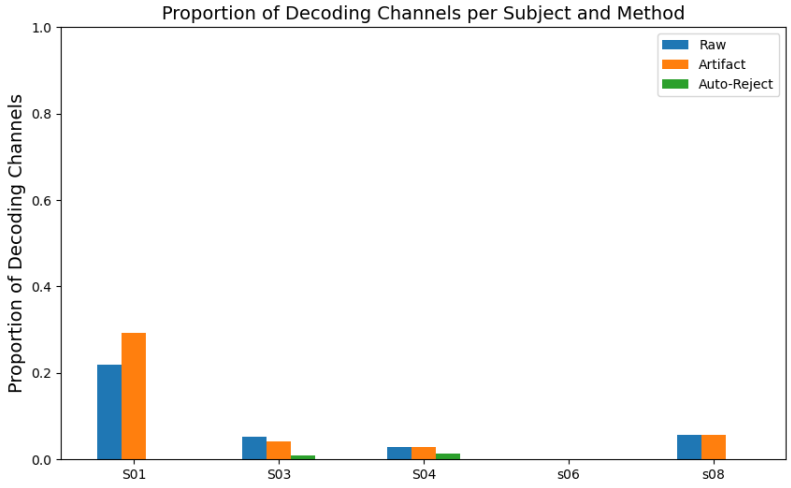

Figure 15. Proportion of decoding channels per method and subject.

Finally, *Figure 15* illustrates how participant s01 is the most influential in this decoding since it has the highest proportion of decoding channels. This result comes from the fact that it has more than a thousand epochs. It can also be seen how participant s06 is not showing any decoding, which suggests the noisy nature of this subject's signal, despite the previous cleaning, impedes its proper decoding.

5.3.2. Multivariate Support Vector Machine

As explained in earlier sections, multivariate decoding differs from univariate since all channels for an epoch are considered when decoding, instead of channel-by-channel, we now look at the combination of all of them. Despite this difference, multivariate SVM starts as the previous univariate method does, by computing the PSD and normalizing it using the same methodology.

Later, to assess decoding accuracy, the function implements k-fold cross-validation with k=5 by default using *Scikit-Learn's* k-fold with shuffling controlled by the provided random state. The SVM pipeline is all incorporated within one same function, although an additional routine is defined within it.

This additional routine parts the feature matrix and angular labels into training and testing sets. Later, in order to prevent any channel from dominating learning due to scale differences a *StandardScaler* is fit on X_{train}, which computes per channel means and standard deviations to normalize it using z-scoring. Because the target angle θ_i is circular, standard support-vector regression must be adapted to respect angle wrapping. To do so, we construct a *Scikit-Learn's* pipeline using the following line: *make_pipeline(AngularRegression(clf=LinearSVR())),* where *LinearSVR()* fits a linear model:

$$\hat{\phi} = w^T x + b,$$

Equation 39. Linear fit for the support-vector regressor.

Where $x \in \mathbb{R}^C$ is a vector of normalized channel powers. The *AngularRegression* wrapper ensures that training and prediction account for circular distance. For each trial, the prediction error is computed via the circular difference:

$$\Delta\theta_i = \angle\left[e^{i(\hat{\theta}_i - \theta_i)}\right].$$

Equation 40. Prediction error computed via circular difference.

The mean absolute error across the test fold is appended to a list, and the average error over all *k* folds is returned as the single-trial decoding error ε_{real}. Once the true error is obtained, we proceed to run the same code for n_{perm} independent permutations $\{\theta(m)\}$ of the original angle vector, and the empirical p-value is computed as the fraction of permuted errors that are less than or equal to the true decoding error.

5.3.2.1. Multivariate analysis results

This decoder was only applied to the manually cleaned data and to the artifact detection's data, since Autoreject has already been discarded in the previous decoder. Previous studies of serial biases in humans had only been conducted through scalp EEG, therefore our iEEG dataset was giving us an opportunity to explore different frequency bands from what we have already seen, nevertheless, the target 2 Hz – 12 Hz showed similar or better results to the other high-frequency bands tested. *Figures 16 and 17* below show the null distribution of errors for subjects s01 and s08, the best performers so far. The results for the other subjects can be found in the *Annex A.*

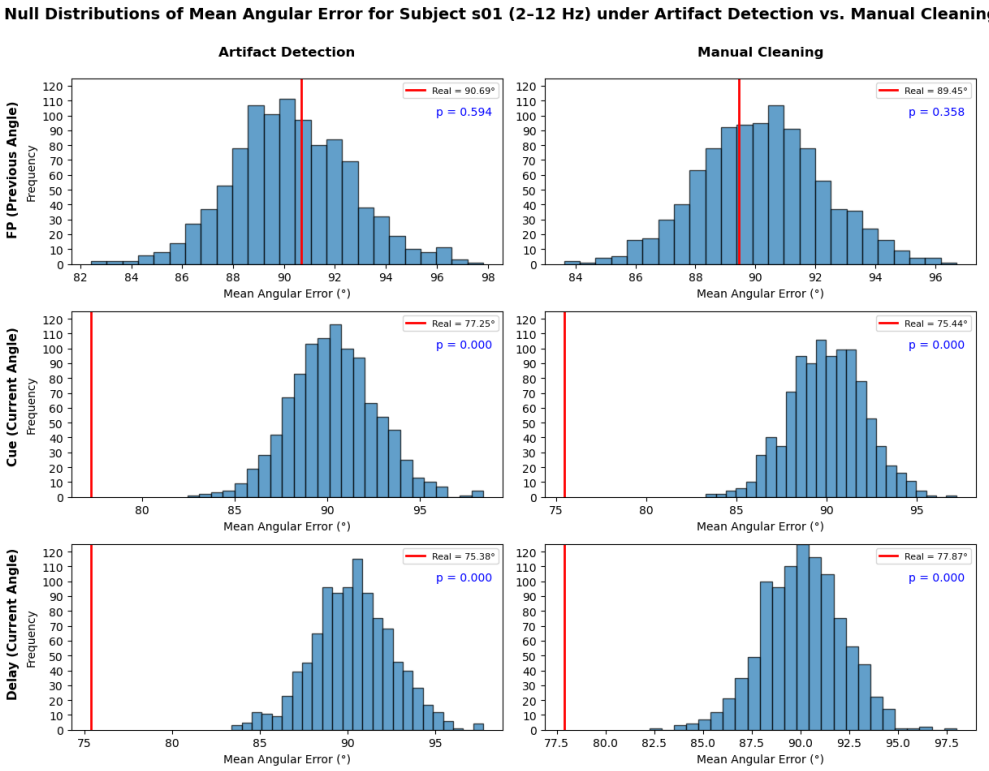

Figure 16. Null distribution histograms of mean angular error using the multivariate SVM for subject s01 and PSD computed for a frequency range of 2 Hz to 12 Hz for 1000 permutations. The first row corresponds to the fixation period decoding for the previous trial stimulus orientation, instead the next two rows (cue and delay) are decoded for the current trial information. Within each panel, the blue bars represent the null distribution of mean angular errors and the red vertical line indicates the actual mean angular error computed on unshuffled data, if the red line appears in the far-left side of the panel away from the null distribution, it means that the actual mean error beats chance level and the decoding is significant.

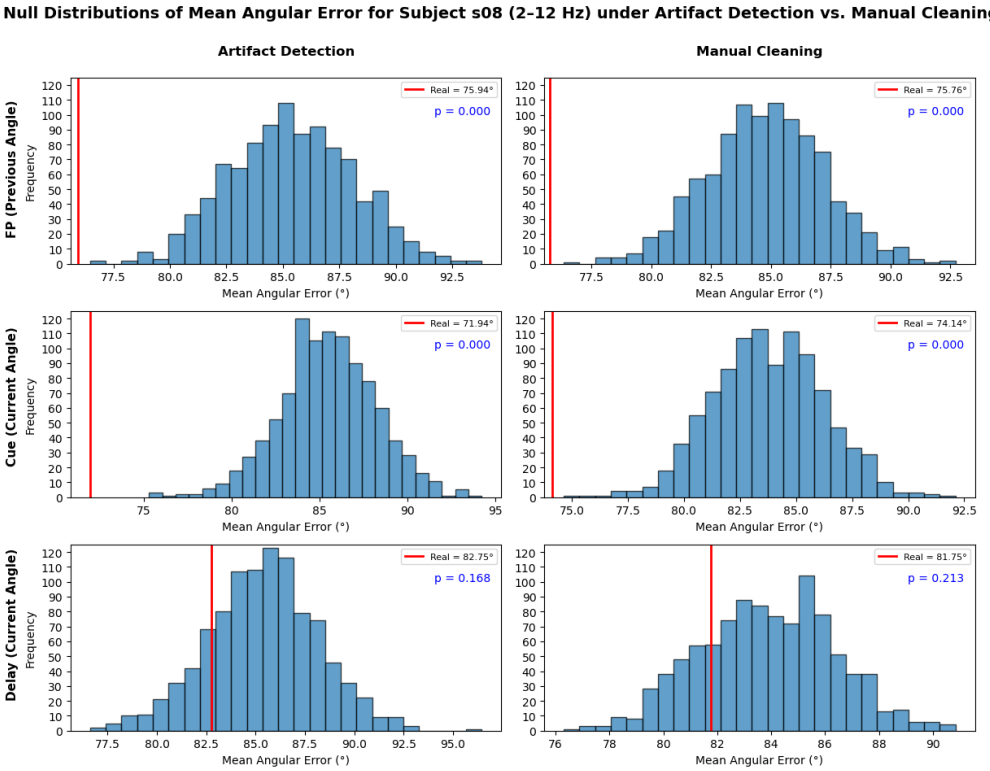

Figure 17. Null distribution histograms of mean angular error using the multivariate SVM for subject s08 and PSD computed for a frequency range of 2 Hz to 12 Hz for 1000 permutations. The first row corresponds to the fixation period decoding for the previous

trial stimulus orientation, instead the next two rows (cue and delay) are decoded for the current trial information. Within each panel, the blue bars represent the null distribution of mean angular errors and the red vertical line indicates the actual mean angular error computed on unshuffled data, if the red line appears in the far-left side of the panel away from the null distribution, it means that the actual mean error beats chance level and the decoding is significant.

We chose to decode the fixation period time window using the previous trial stimulus orientation to look for serial dependency biases and support the bump-attractor model explained in the *Background Section*. As seen in the figures above, for the fixation period, despite s01's larger trial count and stronger univariate modulations, its multivariate decoding lags behind s08's, possibly due to differences in spatial coherence between more than one channel or variability of informative sources. Instead s08's channels may give richer covariance structure for the linear regressor. Both show good decoding results for the cue period time window, although subject s08 shows worst decoding performance for the delay period, possibly due to the same reasons as s01 did in the fixation time window. The results found in subject s08's multivariate fixation period decoding suggest that there are neural correlates of serial dependence mechanisms in iEEG, since when decoding for the previous angle, the true error beats overall chance level indicating that the decoding activity is significant, although the results returned by subject s01 challenge this observation. In order to verify the existence of neural correlates we then applied in *Section 5.3.3* a forward encoding model aiming to solve this contradiction.

As for the preprocessing methods, both show similar results, although for this analysis, all channels available for each pipeline were used, therefore manual cleaning's decoding was performed with higher number of data. Taking this advantage into account, it suggests that these results are consistent with the ones obtained in *Section 5.3.1.5,* supporting the solution proposed in that same section, where for a decoding study where we want to study as many ROIs as we can, manual cleaning offers the best results, although for an analysis of only a small subset of channels or a specific ROI, the custom artifact detection pipeline might offer better results.

5.3.3. Forward encoding

The forward encoding model applied here is designed to work with time-resolved raw data, therefore for this last evaluation no PSD will be computed. Furthermore, this model is meant to show preliminary results only and set a reference point from where this research can continue in the future, therefore, the forward encoding model was only used for the two best performing subjects, s01 and s08.

5.3.3.1. Data partitioning and weight estimation

Firstly, neural data is divided into k=3 k-folds. The forward encoding model assumes that, at each discrete time point *t*, the multichannel sensor data arises from a linear combination of *C* hypothetical orientation channels. For each trial *n*, sensor amplitudes are extracted as $Y_{n,f,t}$ for sensors $f = 1, \dots, F$ and presented orientations are stored in degrees as $\phi_n \in [0,360)$. All orientations are firstly binned in *C* equally spaced bins $G_n \in \{0, \dots, C-1\}$, and each trial's orientation ϕ_n is used to construct a *C*-dimensional design vector via a von Mises function. Concretely, if $\mu_c = 180c/C$ is the preferred angle of channel *c*, we can define the difference:

$$\Delta_{n,c} = (\phi_n - \mu_c)\frac{\pi}{180},$$

Equation 41. Angular difference conversion of presented and preferred orientations to radians.

Through which we can compute the von Mises tuning function:

$$D_{n,c} = \frac{e^{kcos(2\Delta_{n,c})}}{2\pi I_0(k)},$$

Equation 42. Normalized von Mises tuning functions for channel c on trial n.

With a concentration parameter kappa of *k=4,* which controls how sharp is the tuning function's peak around $\Delta_{n,c}$=0, and $I_0(k)$ denotes the modified Bessel function of the first kind. We then design a matrix X by stacking these row-vectors over the training trials and a new sensor matrix Y containing the transposed amplitudes of neural data for those trials.

This model is built on the idea that the pattern of activity across all sensors arises from the activation of *C* hypothetical orientation channels, plus some noise, which can be mathematically described as:

$$y = W^T x + e,$$

Equation 43. Channel activity as a linear combination of orientation-channel activations plus noise.

Where *x* is a *C* dimensional vector of channel activations and *W* is a matrix of unknown weights. In a training set of many trials, we know which is the target activation of the channels, so we find a set of spatial filters *W* that best predict each sensor's value from those channel activations. More specifically, for each channel we perform a linear regression of that channel's known activity onto the recorded sensors, then adjust those weights by applying a shrinkage parameter to the leftover noise. Once this is done and we have *W,* decoding is simple, we just take the filter's rows, normalize them and stack them into a matrix $\widehat{W}$. Therefore, for any new neural data measurement *y* our estimate of the channel activations is simply $\hat{x} = \widehat{W}y$, which when concatenated across all folds returns $\hat{X}_{all}$.

5.3.3.2. Accuracy assessment

To evaluate reconstruction accuracy at each time point *t,* we compute a channel centered tuning matrix $M \in \mathbb{R}^{C\times C}$. In this matrix, the *c*th column is the average of all decoded channel response vector after rotating them so that the true channel *c* appears in the first position. In essence, this matrix answers the following question: When the true channel was *c,* on average how much did channel *c* respond (row 0 of this column), how much did channel one step away respond (row 1), etc.?

$$z_n = \sum_{r=0}^{C-1} e^{ix_r\pi/180}\hat{X}_{all,r,n}, \qquad x_r = G_n\frac{360}{C},$$

Equation 44. Estimated channel responses aggregated into a complex vector.

So that $\theta_n = \arg(z_n)$ is the decoded orientation in degrees. The accuracy measure is:

$$r = \left|\mathbb{E}_n\left[e^{i(\theta_n-\phi_n)^{180}/\pi}\right]\right|.$$

Equation 45. Decoding accuracy of the circular average of angular errors between decoded and true orientations.

Where $\mathbb{E}_n$ is the average taken over all trials *n.* A value of *r* approaching 1 means almost perfect alignment between decoded and actual orientations on every trial, whereas a value closer to 0 indicates chance-level performance.

5.3.3.3. Forward encoding results

During the *Detailed engineering* section, only the results for subject s01, the one who had more data to train the model, will be shown. Nevertheless, the corresponding results to subject s08 can be found in *Annex B*.

Once the forward encoding finishes, we obtain both the time-resolved accuracy *r* and the mean tuning curves along time. These results provide us with two different types of information. Firstly, the accuracy measurement is an indicator of the temporal profile of decodable information, it reveals when neural activity carries reliable information and how strong it is. Secondly, the mean tuning curves, plotted both as a heatmap and as a specific time slice, characterize the shape and sharpness of channel-specific responses, they reflect the fidelity of reconstruction.

This analysis was performed decoding both for the current and the previous orientation stimulus, this way we could observe the decodable information in current trials, and whether there is or not decodable information of previous ones too.

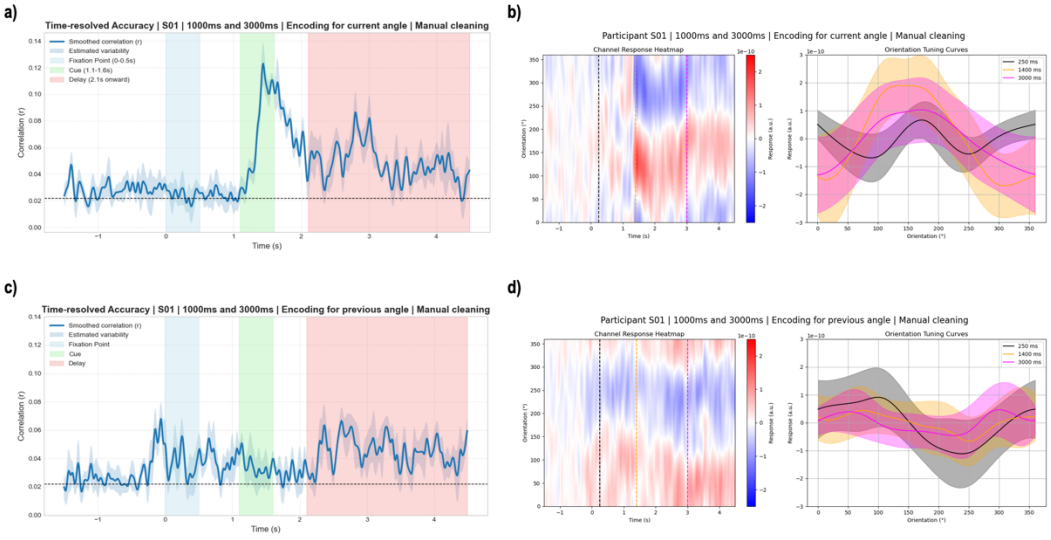

Figure 18. Forward encoding for subject s01's manual cleaning dataset. Where a) and c) represent the time-resolved accuracy during the decoding of the raw manually cleaned signal for the current and previous stimuli respectively. And b) and d) show the tuning curves of the model across time as a heatmap in the left panel, and as a time slice in the right panel. Each time slice corresponds to the dashed line in the heatmap.

As seen in *Figure 18,* there is decodable information in both cases. When decoding for the current trial, neural activity rises when the cue is presented and is maintained all along the delay period as expected. In contrast, neural activity when decoding for the previous trial shows something different, right before the trial starts with the fixation point, there is a sudden burst of decodable information, which slightly fades away to then reappear in the delay period. These findings directly corroborate the reactivation of previous information right before the beginning of a new trial in consistence with the bump-attractor model predictions, explained along *Section 2.2.3* [11]. We also observed a shift in the tuning curve of forward model channels (*Figure 18d*), which suggests that

stimulus information is encoded differently when it's reactivated from the previous trial. This might indicate a coding strategy that allows multiplexing multiple stimuli with different neural codes and minimal interaction. However, this is a preliminary interpretation and should be taken with caution.

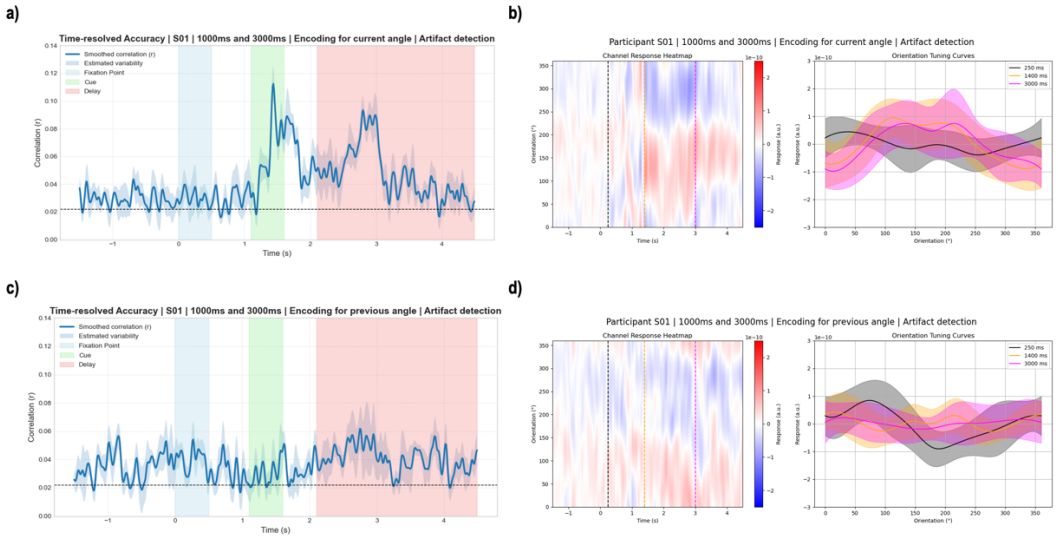

Figure 19. Forward encoding for subject s01's artifact detection dataset. Where a) and c) represent the time-resolved accuracy during the decoding of the raw artifact detection signal for the current and previous stimuli respectively. And b) and d) show the tuning curves of the model across time as a heatmap in the left panel, and as a time slice in the right panel. Each time slice corresponds to the dashed line in the heatmap.

We observed that when using the artifact detection method with the forward encoding model, there seems to be no significant neural activity involved related to the previous stimulus. This observation suggested that some of the channels removed during the artifact cleaning were precisely those conveying the serial bias signals of interest. After this finding, we thought of a possible future method to localize brain regions responsible for maintaining or reactivating information from the previous trial, which consisted of grouping channels within the same ROI and systematically remove one ROI at a time for each analysis from the manual cleaning dataset. By comparing the time course and magnitude of decodable information for both current and previous stimuli under each ROI-omission condition we can infer which anatomical region contributes more to the representation of past-trial information.

This new methodology was only preliminarily applied to subject s01 from the channels missing in the artifact detection dataset. When channels within the intraparietal ROI were excluded from the decoding analysis in subject s01, we observed that the burst of decoding activity in the fixation period still emerged, but subsequently diminished and diffused compared to the intact-channel condition, although decoding activity was still present, this can be seen in *Figure 20* down below. This small attenuation suggests that intraparietal contact carried a small partial component of the serial-bias signal, yet their removal did not abolish decoding activity completely, only diminished it. Thus, although intraparietal cortex appears to contribute slightly to the maintenance or reactivation of previous trial information, it is unlikely to be the sole focus of serial influences. Other ROIs missing from the artifact detection dataset that were also suppressed and made no difference are: middle cingulate, somatosensory, superior temporal, medial parietal and primary motor. Only the intraparietal modified the observed accuracy decoding, unfortunately, no PFC regions were available for this subject.

Most importantly, the ROI-suppression approach provides an initial pathway for localizing the brain regions responsible for serial bias in human iEEG. Because these results come from a single subject with biased electrode implantation, these results remain preliminary. Nevertheless, the fact that intraparietal removal produced a measurable, though incomplete, reduction of decodable past information, indicate that futures studies could implement this method to pinpoint the neural circuits responsible for serial biases.

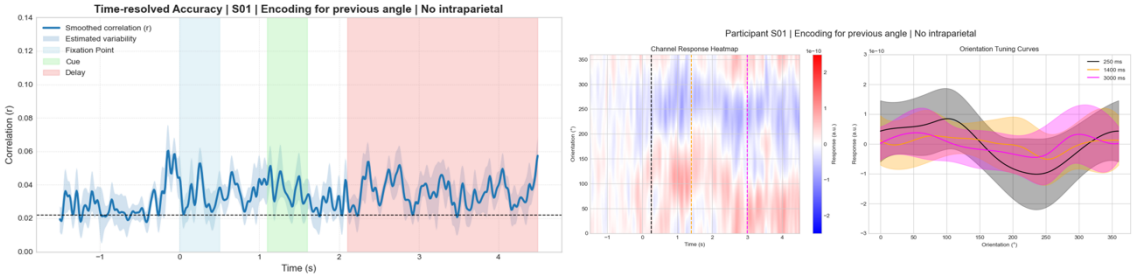

Figure 20. Forward encoding for subject s01's manual cleaning dataset with no intraparietal channels.

6. TECHNICAL VIABILITY

Regardless of the results obtained in the work, to conduct a proper analysis of the technical viability of the project, a SWOT analysis will be carried out. This analysis will identify and develop all parameters that affect the strengths, opportunities, weaknesses, and threats of the project. It is a simple yet powerful tool that helps identify competitive improvement opportunities and work towards enhancing both the project and the team.

	Strengths	Weaknesses
Internal	❖ Institutional collaboration and multidisciplinary team ❖ Access to clinical iEEG data and tested intracranial hardware ❖ Solid foundation of previous research ❖ Mature, open-source Python ecosystem ❖ Scalable batch jobs on cluster	❖ Limited time ❖ Small sample size ❖ Complexity in data anaysis ❖ Dependance on advanced tecnologies ❖ Heterogeneity of electrode coverage ❖ Variable data quality
	Opportunities	**Threats**
External	❖ Clinical and scientific relevance	❖ Economic factors

	❖ Therapeutic applications ❖ Strengthening collaborative networks ❖ Technological innovation	❖ External competition ❖ Pandemics and health crisis ❖ Technical risks

In the following subsections, we will analyze each of these points in more detail.

6.1. Strengths

Strengths refer to the internal initiatives that work well. By analyzing these areas, we can understand what is already functioning correctly. Next, we will analyze the strengths of the project.

- **Institutional collaboration and multidisciplinary team:** The project will be carried out in collaboration with IDIBAPS and Hospital Clínic, enabling access to a large quantity of clinical data and advanced technologies. The involvement of professionals from various disciplines (doctors, engineers, scientists) enables a comprehensive and detailed approach to the problems being investigated.
- **Access to clinical iEEG data and tested intracranial hardware:** There are intracranial EEG equipment and other advanced medical devices, already tested in previous studies. This significantly reduces the cost of the project, allowing the use of highly tested and efficient technological devices.
- **Solid foundation of previous research:** The project is based on prior research performed by the Compte lab, published in high-impact journals.
- **Mature, open-source Python ecosystem:** For the preprocessing pipeline development, many well-established Python libraries as MNE-Python, NumPy and SciPy among others are used, which allows for a faster and safer development of the script.
- **Scalable batch jobs on cluster:** Once a reproducible automated pipeline for one subject is completed, parallel jobs can be sent to work in the cluster for the rest of the subjects.

6.2. Weaknesses

Weaknesses refer to internal initiatives that are not functioning adequately. Identifying them provides a starting point for improving the project.

- **Limited time:** The project's timeframe as an undergraduate thesis imposes significant restrictions, limiting the possibility of conducting long-term studies and defining a specific deadline.
- **Small sample size:** The limited availability of patients who can participate in the study, either due to a lack of willingness from the patients or a lack of financial resources from the researchers, can affect the accuracy of the results.

- **Complexity in data analysis:** The processing and analysis of intracranial EEG data is complex and requires significant time and resources.
- **Dependence on advanced technologies:** The high costs and potential lack of specialized equipment may delay the project or hinder its continuity.
- **Heterogeneity of electrode coverage:** Since each patient has different implantation targets, analysis may not be completely directed towards brain areas of interest for this project.
- **Variable data quality:** Intracranial recordings often contain high-amplitude artifacts due to movement, muscle twitches, line noise and even epileptic activity in our situation, hence requiring extensive cleaning, slowing the pipeline and losing the little data available. Despite noise being qualified as a weakness, it is also a big motivation behind this project and one of the main objective drivers.

6.3. Opportunities

Opportunities are the strengths and weaknesses, along with any external initiatives that will place us in a stronger competitive position. These are factors that can benefit the project's development. They might include weaknesses to be improved, or other areas not identified in the first two stages of the analysis.

- **Clinical and scientific relevance:** The study of working memory and serial biases in patients with neuropsychiatric disorders is a growing and highly interesting field of research.
- **Therapeutic applications:** The project's findings could help identify new therapeutic targets and treatment strategies to improve cognitive deficits in patients with schizophrenia and anti-NMDAR encephalitis.
- **Strengthening collaborative networks:** Collaboration with prestigious institutions, such as Hospital Clínic and IDIBAPS, can open doors to future research projects and funding opportunities.
- **Technological innovation:** The use of advanced techniques and the potential to develop new methodologies can position the research team as a leader in the field.

6.4. Threats

Threats refer to areas that have the potential to cause problems and jeopardize the success of the project. They differ from weaknesses in that threats are external and generally beyond our control.

- **Economic factors:** The high costs associated with the use of advanced equipment and the possible need for maintenance or replacement can affect the project’s budget.
- **External competition:** Other research groups with access to broader resources and larger datasets could produce more accurate and quicker results.
- **Pandemics and health crises:** Situations like the COVID-19 pandemic can disrupt patient access, data collection, and coordination among the professionals involved.

- **Technical risks:** The possibility of technical errors in the intracranial EEG equipment or data analysis platforms can cause significant delays.

7. EXECUTION SCHEDULE

An execution plan is essential in any project. It provides a detailed and structured guide to reach the project's objectives in an efficient and effective way. An execution schedule clearly defines the needed steps to complete the project. It helps to break down complex tasks into simpler ones, allowing a better comprehension and execution. It also helps to assign resources, including time, personnel and budget. Additionally, with tools like PERT or GANTT diagrams, time can be managed and monitored effectively.

7.1. WBS Dictionary

By breaking down work into smaller, manageable and approachable tasks productivity is optimized. For projects, the Work Breakdown Structure (WBS) is the tool that uses this technique and is one of the most important project management documents. It integrates scope, cost and schedule baselines ensuring that project plans are in alignment. In *Figure 21*, the WBS made for this project is shown.

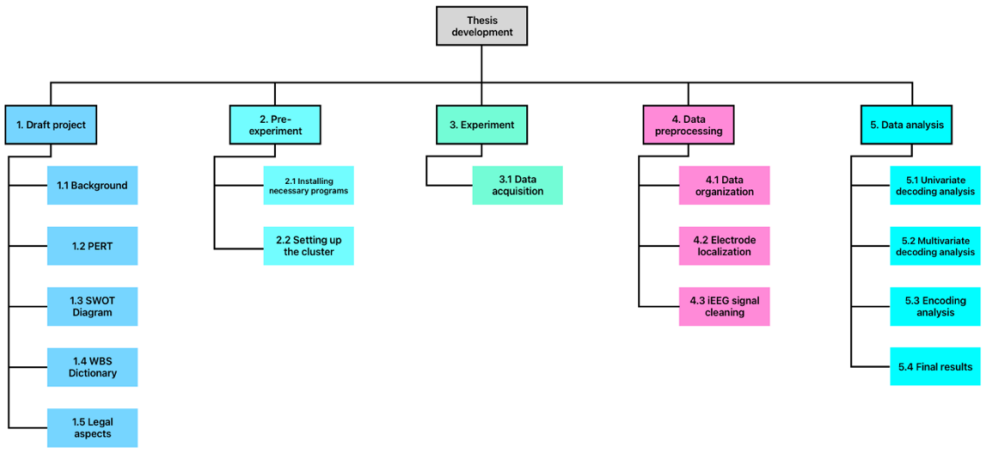

Figure 21. WBS Diagram.

A thorough analysis of each task has been conducted to create the WBS dictionary. A detailed description of each task can be found in the *Annex C.*

7.2. PERT Diagram

It is important to know which tasks are dependent on other ones and how much time does it take to complete each one of them. A PERT chart is a network diagram that allows project managers to create project schedules. They're used in the Program Evaluation Review Technique (PERT) to represent a project's timeline, estimate the duration of tasks, identify task dependencies and find the critical path of a project. To do the diagram, the different tasks defined in the WBS and the dependencies between them are represented in the following table.

Task	Code	Letter	Duration (days)	Precedents
Background	1.1	A	5	-
PERT+GANTT	1.2	B	4	D
SWOT diagram	1.3	C	1	D
WBS dictionary	1.4	D	3	-
Legal aspects	1.5	E	2	D
Install necessary programs	2.1	F	1	D
Setting up the cluster	2.2	G	1	F
Data acquisition	3.1	H	60	E
Data organization	4.1	I	5	G, H
Electrode localization	4.2	J	30	I
iEEG signal cleaning	4.3	K	60	I
Univariate decoding analysis	5.1	L	30	J, K
Multivariate decoding analysis	5.2	M	30	K
Encoding analysis	5.3	N	30	J, K
Final results	5.4	O	5	L, M, N

Table 2. Identification, precedents and timing of tasks.

Subsequently, using *Table 2*, we can create a PERT diagram which will help identify the critical path. This process requires the identification or early and late times for each activity. Following the forward pass, we can determine the early start time, which indicates the earliest an activity can start, and early finish time, the earliest it can end based on our schedule. Then, thanks to the backward pass, we can get the late start and late finish, the latest an activity can start or finish without increasing the duration of the entire project. It can be seen in *Figure 22*, that the late finish and early finish in activities D, E, H, I, K, L, M, N and O is the same, which implies that these tasks correspond to the critical path, meaning that if we were to delay any of them, we would have to increase the entire duration of the project, this critical path is highlighted in the arrows in red.

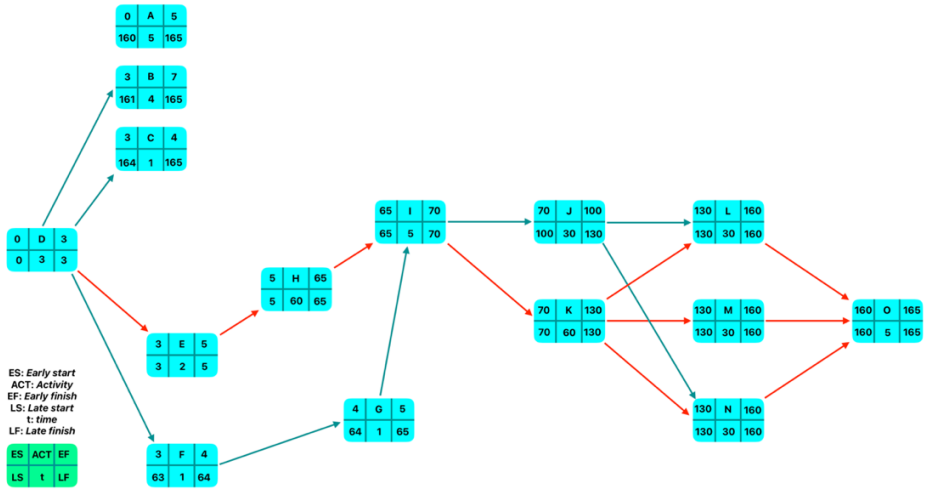

Figure 22. PERT Diagram.

7.3. GANTT Diagram

Thanks to the GANTT Diagram, we are able to control tasks of the project over time, thereby facilitating following and tracking activities. Time is represented on the *x-axis* and the activities appear in the *y-axis.* In *Figure 23*, the GANTT diagram for our project is represented.

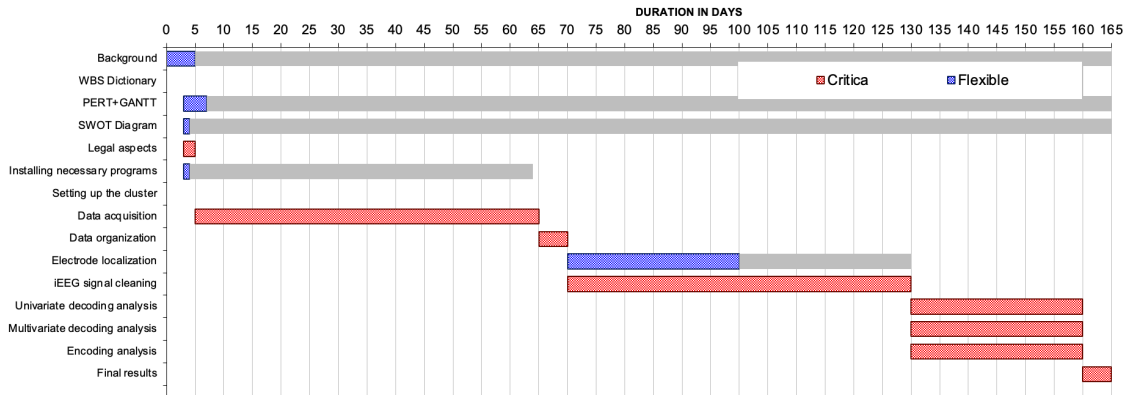

Figure 23. GANTT Diagram

8. ECONOMICAL VIABILITY

For the correct development of the project, the consideration of multiple costs is required. These costs can be categorized in the following groups:

- Material and infrastructure resources.
- Subject related resources
- Human resources.

8.1. Materials and infrastructure resources

Firstly, we will analyze the physical and infrastructure elements needed to carry out the project. This includes equipment, programs and software licenses:

	Item	Units	Price / unit (€)	Total price (€)
Material resources	Implantable electrodes	10u x 15 subjects = 150	2.500€	375.000€
	EEG receptor and amplifier	1	25.000€	25.000€
	Eye tracker	1	5.000€	5.000€
	Laptop	1	950€	950€
	Screen	1	200€	200€
Infrastructure	High-performance computing cluster	1	38.985€	38.985€
	Total			414.700€

Table 3. Material and software prices broken down.

Additionally, all data preprocessing and analyses were performed on the laboratory's previously acquired high-performance computing cluster, it is included in the pricing list for reference, although

it did not suppose an additional expense for project, therefore it will not be considered for the overall total costs.

8.2. Subject related resources

In a clinical trial, it is crucial to consider the costs related to subjects. For this calculus, we will consider that we are going to be studying 15 subjects, even though at the end we only analyzed 5 of them. Also, each patient remains hospitalized an average of 3 weeks in the hospital, that being a total of 504 hours.

Activity	Hours/subject	Total hours	Cost/hour (€)	Total cost (€)
Compensation to subjects (volunteer)	5	5h * 15 = 75h	0	0
Patient maintenance in the hospital	504	504h * 15 = 7560h	20	151.200
Experimental session	5	75h	10	750
Total				151.950

Table 4. Subject related expenses.

8.3. Human resources

Finally, the cost of the personal involved in the project also needs to be considered. The costs for the thesis student have been allocated according to the average salary of a project engineer, which is approximately 35,000€ per year, moreover, the standardized time schedule to complete a 12 ECTS consists of 300 official hours.

Item	Total hours	Cost/hour (€)	Total cost (€)
Thesis director	100	20	2.000
Thesis tutor	100	20	2.000
Technical staff	40	15	600
Thesis student	300	12	3600
Total			8200

Table 5. Total hours and hourly pay for human resources, including total cost in euros.

8.4. Total costs

After examining the various expenses, we will aggregate them to determine the total funds required to complete the project. These details are shown in *Table 6*. It is important to recognize that this is a budget estimate for conducting the work from beginning to end under normal conditions. However, much of the equipment used had already been acquired for previous experiments and will be utilized in future tests as well. Additionally, as mentioned before, the costs for the professionals involved in the project are approximate estimates.

Item	Total cost (€)
Material	414.700
Subject related resources	151.950
Human resources	8200
Total	574.850

Table 6. Total costs for the project divided in sections and summed up.

9. REGULATIONS AND LEGAL ASPECTS

The development of this project involves compliance with various regulations and laws that ensure the ethics, safety, and legality of the research, especially considering that it involves sensitive data and human patients. Below are the main regulations and legal aspects applicable, and in *Annex D* we can find the consent form given to the participants.

9.1. Ethical and clinical investigation regulations

To comply with ethical principles for biomedical research in human subjects, including respect for all individuals and protection of their health by ensuring informed consent and patient well-being, every study involving human subjects must adhere to various guidelines. These include the Declaration of Helsinki, the Biomedical Research Law (Ley 14/2007) [45], which states that all biomedical studies must obtain approval from a Research Ethics Committee (CEI). Also significant are the guidelines of Good Clinical Practice, international standards of ethical and scientific quality, and the Clinical Trials Law (Real Decreto 1090/2015) [46], which regulates the conduct of clinical trials in Spain.

9.2. Regulations on data and technology usage

Considering that our study involves dealing with sensitive patient data, it is mandatory to comply with regulations such as the General Data Protection Regulation (GDPR, Regulation (EU) 2016/679) [47], originating from the EU and regulating the protection of personal data and individuals' privacy. The Organic Law on Data Protection and Digital Rights Guarantee (LOPDGDD, Ley Orgánica 3/2018) [48], an extension of the GDPR, must also be considered. Additionally, specific regulations on the use of medical devices and healthcare technologies, such as the CE marking for medical devices in Europe, must be followed. These regulations are provided by Regulation (EU) 2021/2282 [49]. Considering that our study will involve various medical technologies, such as iEEG equipment, among others, we must ensure that such equipment complies with the regulations, ensuring their safety and effectiveness.

In summary, the project must adhere to a strict regulatory framework that ensures the ethics and legality of the research. Compliance with these laws and regulations not only ensures the protection of participants but also strengthens the validity and credibility of the results obtained.

10. CONCLUSIONS AND FUTURE LINES

This study aimed to evaluate the efficacy of three preprocessing strategies in optimizing iEEG data for decoding: manual cleaning or eye-guided artifact removal, a custom artifact-detection, and the Autoreject pipeline. Although the primary focus was the previously studied 2 Hz – 12 Hz frequency band, all available frequency ranges were studied to determine whether supplemental bands would offer reliable decoding, although they returned similar or worse results. A further aim was to corroborate the presence of serial dependencies in human intracranial studies and set a roadmap for future investigations to localize the brain regions controlling them.

In summary, the custom artifact detection approach returned marginally superior univariate results compared to the manual cleaning method in both the target low-frequency band and the high-gamma band, which demonstrated enhanced sensitivity to both current-trial and residual past-trial information. However, the gains afforded by artifact detection did not overwhelmingly outweigh the ones offered by a simpler manual hybrid cleaning to compensate for the amount of trials and channels lost. If when using the artifact detection method we prefer to conserve more data, it would be necessary to increase significantly the median absolute deviation threshold, at the risk of decreasing sensitivity. Autoreject's-consensus based thresholds proved insufficiently flexible to accommodate the spatial heterogeneity of human iEEG configurations. These results indicate that aggressive automated rejection is not always best when a broad, global study of all ROIs is desired. Applying an automated cleaning pipeline can result more favorable when only a small subset of channels or a specific ROI is studied, this way more data is kept while enhancing the signal-to-noise ratio.

The most robust neural signatures of the present stimuli in the univariate circular correlation emerged within the temporal and frontal regions for current trials, whereas residual information reappeared in occipital and parietal cortices during fixation periods. These observations, together with the results offered by the forward encoding model, align with the bump-attractor model of working memory by revealing a reactivation of latent synaptic representation shortly before the fixation period. When the forward encoding model was restricted to a set of ROIs, decodable traces of previous-trial information were slightly attenuated, in particular when the intraparietal region was omitted for subject s01. This findings might imply that serial-dependency signals might be distributed rather than localized exclusively to a single cortical locus.

Two main limitations apply to this study which avoid the generalization of these findings. Firstly, reliance on data from epileptic patients introduce a sampling bias, clinical considerations determined electrode placements, limiting coverage across all cortical regions. Second, the small number of usable subjects, owing in part to data quality and recording issues, constrains statistical power.

Future studies should therefore adopt flexible, context-dependent preprocessing strategies. For investigations that aim to study distributed cortical substrates across multiple ROIs, manual eye-guided cleaning remains the preferred approach, as it preserves the maximal number of channels and epochs without sacrificing performance. Instead, when the research questions are confined to a single ROI or a small subset of channels, artifact detection may be preferable, since it has been proven that it slightly improves decoding accuracy. It has also been seen how participants with a

larger number of trials perform significantly better in decoding studies, this results also align with the previous research explain is *Section* 2.2.5, where it is explained how prioritizing obtaining more data may be preferable to focusing on cleaning the already existing one. Expanding the patient cohort with more diverse electrode implantations will be essential to validate the anatomical regions behind serial biases. Systematic application of ROI-suppression with a larger sample will clarify whether regions such as the intraparietal sulcus consistently mediate reactivation of past information or whether a boarder network of parietal, frontal or temporal areas contributes in a subject specific manner.

Ultimately, by balancing data preservation and signal fidelity, and by preliminarily delineating the ROIs implicated in serial dependencies, this study both advances in current decoding approaches and defines a clear path for future efforts to discover the brain regions and mechanisms behind it.

11. REFERENCES

[1] Defelipe, J. (2011). The evolution of the brain, the human nature of cortical circuits, and intellectual creativity. *Frontiers in Neuroanatomy*, *5*, 29. https://doi.org/10.3389/fnana.2011.00029

[2] Bem Junior, L. S., Lemos, N. B., de Lima, L. F. G., Dias, A. J. A., Neto, O. da C. F., de Lira, C. C. S., Diniz, A. M. S., Rabelo, N. N., Barroso, L. K. V., Valença, M. M., & de Azevedo Filho, H. R. C. (2021). The anatomy of the brain - learned over the centuries. *Surgical Neurology International*, *12*(319), 319. https://doi.org/10.25259/SNI_200_2021

[3] Nejedly, P., Kremen, V., Sladky, V., Cimbalnik, J., Klimes, P., Plesinger, F., Mivalt, F., Travnicek, V., Viscor, I., Pail, M., Halamek, J., Brinkmann, B. H., Brazdil, M., Jurak, P., & Worrell, G. (2020). Multicenter intracranial EEG dataset for classification of graphoelements and artifactual signals. *Scientific Data*, *7*(1), 179. https://doi.org/10.1038/s41597-020-0532-5

[4] Pascucci, D., Tanrikulu, Ö. D., Ozkirli, A., Houborg, C., Ceylan, G., Zerr, P., Rafiei, M., & Kristjánsson, Á. (2023). Serial dependence in visual perception: A review. *Journal of Vision*, *23*(1), 9. https://doi.org/10.1167/jov.23.1.9

[5] Goldman-Rakic, P. S. (1995). Cellular basis of working memory. *Neuron*, *14*(3), 477–485. https://doi.org/10.1016/0896-6273(95)90304-6

[6] Funahashi, S., Bruce, C. J., & Goldman-Rakic, P. S. (1989). Mnemonic coding of visual space in the monkey's dorsolateral prefrontal cortex. *Journal of Neurophysiology*, *61*(2), 331–349. https://doi.org/10.1152/jn.1989.61.2.331

[7] Mongillo, G., Barak, O., & Tsodyks, M. (2008). Synaptic theory of working memory. *Science (New York, N.Y.)*, *319*(5869), 1543–1546. https://doi.org/10.1126/science.1150769

[8] Rose, N. S., LaRocque, J. J., Riggall, A. C., Gosseries, O., Starrett, M. J., Meyering, E. E., & Postle, B. R. (2016). Reactivation of latent working memories with transcranial magnetic stimulation. *Science (New York, N.Y.)*, *354*(6316), 1136–1139. https://doi.org/10.1126/science.aah7011

[9] Stokes, M. G. (2015). "Activity-silent" working memory in prefrontal cortex: a dynamic coding framework. *Trends in Cognitive Sciences*, *19*(7), 394–405. https://doi.org/10.1016/j.tics.2015.05.004

[10] Zucker, R. S., & Regehr, W. G. (2002). Short-term synaptic plasticity. *Annual Review of Physiology*, *64*(1), 355–405. https://doi.org/10.1146/annurev.physiol.64.092501.114547

[11] Barbosa, J., Stein, H., Martinez, R. L., Galan-Gadea, A., Li, S., Dalmau, J., Adam, K. C. S., Valls-Solé, J., Constantinidis, C., & Compte, A. (2020). Interplay between persistent activity and activity-silent dynamics in the prefrontal cortex underlies serial biases in working memory. *Nature Neuroscience*, *23*(8), 1016–1024. https://doi.org/10.1038/s41593-020-0644-4

[12] Gallant, J. (n.d.). *Encoding and decoding with voxel-wise models*. Brainmapping.org. Retrieved June 5, 2025, from

https://brainmapping.org/NITP/images/Summer2014Slides/20140728_EncodingAndDecoding_Gallant.pdf

[13] Kohn, A. (2007). Visual adaptation: physiology, mechanisms, and functional benefits. *Journal of Neurophysiology*, *97*(5), 3155–3164. https://doi.org/10.1152/jn.00086.2007

[14] Fischer, J., & Whitney, D. (2014). Serial dependence in visual perception. *Nature Neuroscience*, *17*(5), 738–743. https://doi.org/10.1038/nn.3689

[15] Fritsche, M., Mostert, P., & de Lange, F. P. (2017). Opposite effects of recent history on perception and decision. *Current Biology: CB*, *27*(4), 590–595. https://doi.org/10.1016/j.cub.2017.01.006

[16] Stein, H., Barbosa, J., Soldevilla, D. L., Rosa-Justicia, M., Morató, A., Galan-Gadea, A., Prades, L., Muñoz-Lopetegui, A., Ariño, H., Martinez-Hernandez, E., Guasp, M., Castro-Fornieles, J., Dalmau, J., Santamaria, J., & Compte, A. (2024). Neural signatures of reduced serial dependence in anti-NMDAR encephalitis and schizophrenia. In *PsyArXiv*. https://doi.org/10.31234/osf.io/kz73s

[17] Stein, H., Barbosa, J., Rosa-Justicia, M., Prades, L., Morató, A., Galan-Gadea, A., Ariño, H., Martinez-Hernandez, E., Castro-Fornieles, J., Dalmau, J., & Compte, A. (2020). Reduced serial dependence suggests deficits in synaptic potentiation in anti-NMDAR encephalitis and schizophrenia. *Nature Communications*, *11*(1), 4250. https://doi.org/10.1038/s41467-020-18033-3

[18] Nguyen, L., & Wang, C. (2023). Anti-NMDA receptor autoimmune encephalitis: Diagnosis and management strategies. *International Journal of General Medicine*, *16*, 7–21. https://doi.org/10.2147/IJGM.S397429

[19] Nakazawa, K., & Sapkota, K. (2020). The origin of NMDA receptor hypofunction in schizophrenia. *Pharmacology & Therapeutics*, *205*(107426), 107426. https://doi.org/10.1016/j.pharmthera.2019.107426

[20] Meisler, S. L., Kahana, M. J., & Ezzyat, Y. (2019). Does data cleaning improve brain state classification? *Journal of Neuroscience Methods*, *328*(108421), 108421. https://doi.org/10.1016/j.jneumeth.2019.108421

[21] Delorme, A. (2023). EEG is better left alone. *Scientific Reports*, *13*(1), 2372. https://doi.org/10.1038/s41598-023-27528-0

[22] Nuno, A., Suarez, J., Le Bars, M. (2023, Februrary 14) Sizing the brain. Deloitte. Insights. https://www2.deloitte.com/uk/en/insights/industry/health-care/global-neuroscience-market-investment-report.html

[23] *Localizing electrodes using a 3D-scanner*. (2025, February 5). FieldTrip Toolbox. https://www.fieldtriptoolbox.org/tutorial/source/electrode/

[24] *ielvis [licensed for non-commercial use only] / FrontPage*. (n.d.). Pbworks.com. Retrieved May 23, 2025, from http://ielvis.pbworks.com/w/page/116347253/FrontPage

[25] *Tutorials/leegContactLocalization - Brainstorm*. (n.d.). Usc.edu. Retrieved May 23, 2025, from https://neuroimage.usc.edu/brainstorm/Tutorials/leegContactLocalization

[26] Wang, Z., Magnotti, J. F., Zhang, X., & Beauchamp, M. S. (2023). YAEL: Your Advanced Electrode Localizer. *eNeuro*, *10*(10). https://doi.org/10.1523/ENEURO.0328-23.2023

[27] Tibdewal, M. N., Mahadevappa, M., Ray, A. K., Malokar, M., & Dey, H. R. (2016). Power line and ocular artifact denoising from EEG using notch filter and wavelet transform. *2016 3rd International Conference on Computing for Sustainable Global Development (INDIACom)*, 1654–1659.

[28] Widmann, A., Schröger, E., & Maess, B. (2015). Digital filter design for electrophysiological data--a practical approach. *Journal of Neuroscience Methods*, *250*, 34–46. https://doi.org/10.1016/j.jneumeth.2014.08.002

[29] Ranjan, R. K., Choubey, C. K., Nagar, B. C., & Paul, S. K. (2016). Comb filter for elimination of unwanted power line interference in biomedical signal. *Journal of Circuits Systems and Computers*, *25*(06), 1650052. https://doi.org/10.1142/s0218126616500523

[30] *b. Re-referencing*. (n.d.). EEGLAB Wiki. Retrieved May 24, 2025, from https://eeglab.org/tutorials/05_Preprocess/rereferencing.html

[31] *mne.set_bipolar_reference — MNE 1.9.0 documentation*. (n.d.). Mne.Tools. Retrieved May 24, 2025, from https://mne.tools/stable/generated/mne.set_bipolar_reference.html

[32] Kelly, J. W., Siewiorek, D. P., Smailagic, A., & Wang, W. (2013). Automated filtering of common-mode artifacts in multichannel physiological recordings. *IEEE Transactions on Bio-Medical Engineering*, *60*(10), 2760–2770. https://doi.org/10.1109/TBME.2013.2264722

[33] Zhai, Y., & Yao, D. (2004). A study on the reference electrode standardization technique for a realistic head model. *Computer Methods and Programs in Biomedicine*, *76*(3), 229–238. https://doi.org/10.1016/j.cmpb.2004.07.002

[34] Jas, M., Engemann, D. A., Bekhti, Y., Raimondo, F., & Gramfort, A. (2017). Autoreject: Automated artifact rejection for MEG and EEG data. *NeuroImage*, *159*, 417–429. https://doi.org/10.1016/j.neuroimage.2017.06.030

[35] Fields, E. C., & Kuperberg, G. R. (2020). Having your cake and eating it too: Flexibility and power with mass univariate statistics for ERP data. *Psychophysiology*, *57*(2), e13468. https://doi.org/10.1111/psyp.13468

[36] Holdgraf, C. R., Rieger, J. W., Micheli, C., Martin, S., Knight, R. T., & Theunissen, F. E. (2017). Encoding and decoding models in cognitive electrophysiology. *Frontiers in Systems Neuroscience*, *11*, 61. https://doi.org/10.3389/fnsys.2017.00061

[37] (N.d.). Mathworks.com. Retrieved May 14, 2025, from https://www.mathworks.com/discovery/notch-filter.html

[38] Analog Devices, Inc. (2006). *Basic linear design* (Chapter 8). Analog Devices. https://www.analog.com/media/en/training-seminars/design-handbooks/basic-linear-design/chapter8.pdf

[39] Nassar, S. R., Eisa, A. A., Saleh, A. A., Farahat, M. A., & Abdel-Gawad, A. F. (2020). Evaluating the impact of connected non linear loads on power quality- a nuclear reactor case study. *Journal of Radiation Research and Applied Sciences*, *13*(1), 688–697. https://doi.org/10.1080/16878507.2020.1828018

[40] Welch, P. (1967). The use of fast Fourier transform for the estimation of power spectra: A method based on time averaging over short, modified periodograms. *IEEE Transactions on Audio and Electroacoustics*, *15*(2), 70–73. https://doi.org/10.1109/tau.1967.1161901

[41] So, H., Chan, Y., Ma, Q., & Ching, P. (1999). Comparison of various periodograms for sinusoid detection and frequency estimation. *IEEE Transactions on Aerospace and Electronic Systems*, *35*, 945–952. https://doi.org/10.1109/7.784064

[42] Staresina, B. P., Bergmann, T. O., Bonnefond, M., van der Meij, R., Jensen, O., Deuker, L., Elger, C. E., Axmacher, N., & Fell, J. (2015). Hierarchical nesting of slow oscillations, spindles and ripples in the human hippocampus during sleep. *Nature Neuroscience*, *18*(11), 1679–1686. https://doi.org/10.1038/nn.4119

[43] Jas, M., Engemann, D. A., Bekhti, Y., Raimondo, F., & Gramfort, A. (2017). Autoreject: Automated artifact rejection for MEG and EEG data. *NeuroImage*, *159*, 417–429. https://doi.org/10.1016/j.neuroimage.2017.06.030

[44] *Autoreject — autoreject 0.4.2 documentation. (n.d.). Github.Io. Retrieved May 23, 2025, from https://autoreject.github.io/stable/index.html*

[45] *BOE-A-2007-12945 Ley 14/2007, de 3 de julio, de Investigación biomédica*. (2007). Boe.es. Retrieved June 2, 2025, from https://www.boe.es/buscar/doc.php?id=BOE-A-2007-12945

[46] *BOE-A-2015-14082 Real Decreto 1090/2015, de 4 de diciembre, por el que se regulan los ensayos clínicos con medicamentos, los Comités de Ética de la Investigación con medicamentos y el Registro Español de Estudios Clínicos*. (2015). Boe.es. Retrieved June 2, 2025, from https://www.boe.es/buscar/doc.php?id=BOE-A-2015-14082

[47] *Regulation - 2016/679 - EN - gdpr - EUR-Lex*. (2016). Europa.Eu. Retrieved June 2, 2025, from https://eur-lex.europa.eu/eli/reg/2016/679/oj/eng

[48] *BOE-A-2018-16673 Ley Orgánica 3/2018, de 5 de diciembre, de Protección de Datos Personales y garantía de los derechos digitales*. (2018). Boe.es. Retrieved June 2, 2025, from https://www.boe.es/buscar/act.php?id=BOE-A-2018-16673

[49] *Regulation - 2021/2282 - EN - EUR-Lex*. (n.d.). Europa.Eu. Retrieved June 2, 2025, from https://eur-lex.europa.eu/eli/reg/2021/2282/oj/eng

12. ANNEXES

Annex A. Multivariate SVM results for subjects s03, s04 and s06

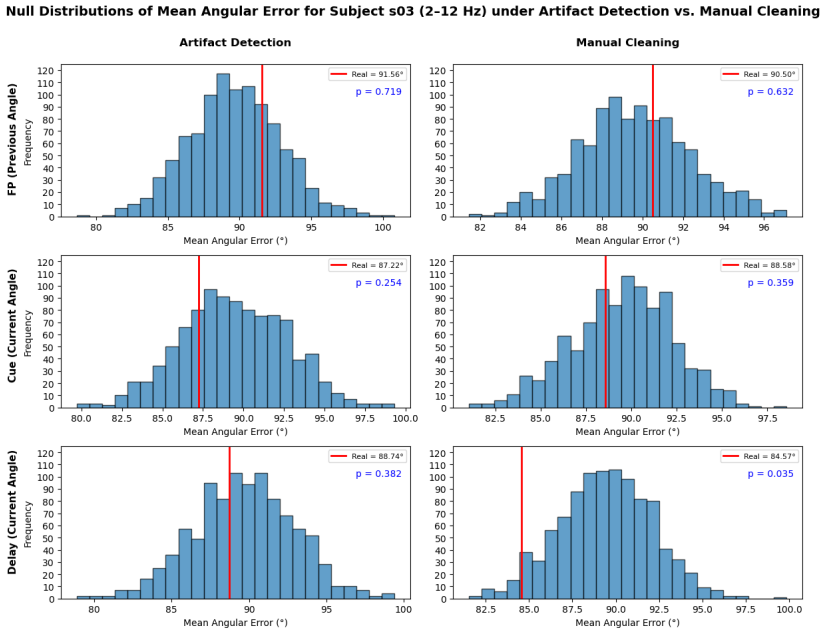

Figure 24. Null distribution histograms of mean angular error using the multivariate SVM for subject s03 and PSD computed for a frequency range of 2 Hz to 12 Hz for 1000 permutations. The first row corresponds to the fixation period decoding for the previous trial stimulus orientation, instead the next two rows (cue and delay) are decoded for the current trial information. Within each panel, the blue bars represent the null distribution of mean angular errors and the red vertical line indicates the actual mean angular error computed on unshuffled data, if the red line appears in the far-left side of the panel away from the null distribution, it means that the actual mean error beats chance level and the decoding is significant.

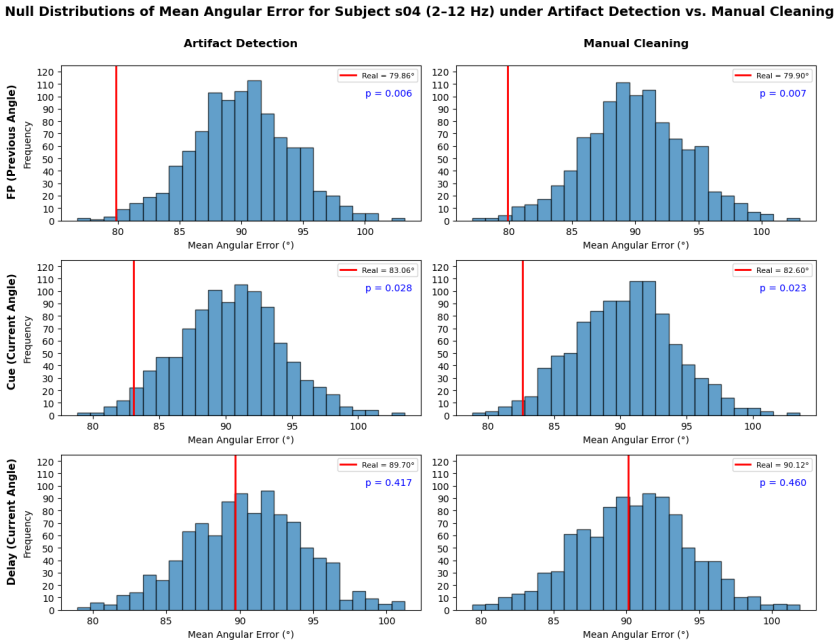

Figure 25. Null distribution histograms of mean angular error using the multivariate SVM for subject s04 and PSD computed for a frequency range of 2 Hz to 12 Hz for 1000 permutations. The first row corresponds to the fixation period decoding for the previous trial stimulus orientation, instead the next two rows (cue and delay) are decoded for the current trial information. Within each panel, the blue bars represent the null distribution of mean angular errors and the red vertical line indicates the actual mean angular error

computed on unshuffled data, if the red line appears in the far-left side of the panel away from the null distribution, it means that the actual mean error beats chance level and the decoding is significant.

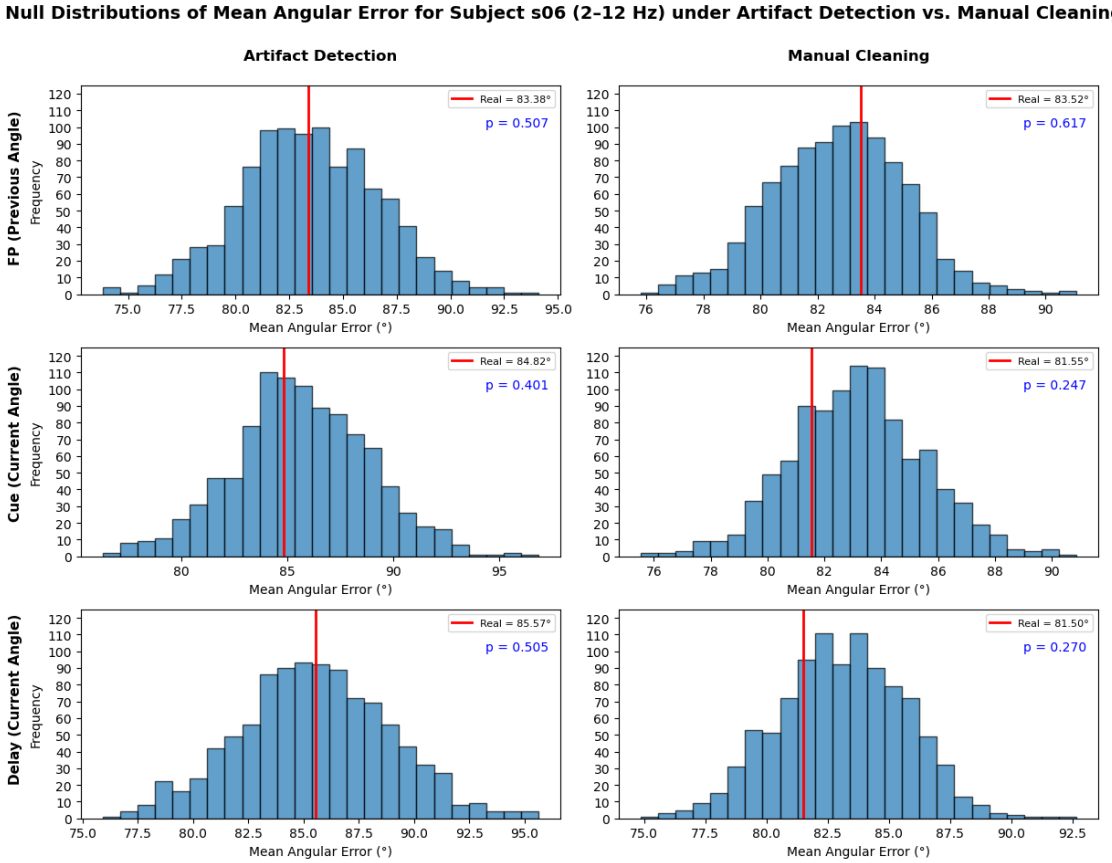

Figure 26. Null distribution histograms of mean angular error using the multivariate SVM for subject s06 and PSD computed for a frequency range of 2 Hz to 12 Hz for 1000 permutations. The first row corresponds to the fixation period decoding for the previous trial stimulus orientation, instead the next two rows (cue and delay) are decoded for the current trial information. Within each panel, the blue bars represent the null distribution of mean angular errors and the red vertical line indicates the actual mean angular error computed on unshuffled data, if the red line appears in the far-left side of the panel away from the null distribution, it means that the actual mean error beats chance level and the decoding is significant.

Annex B. Forward encoding model results for s08

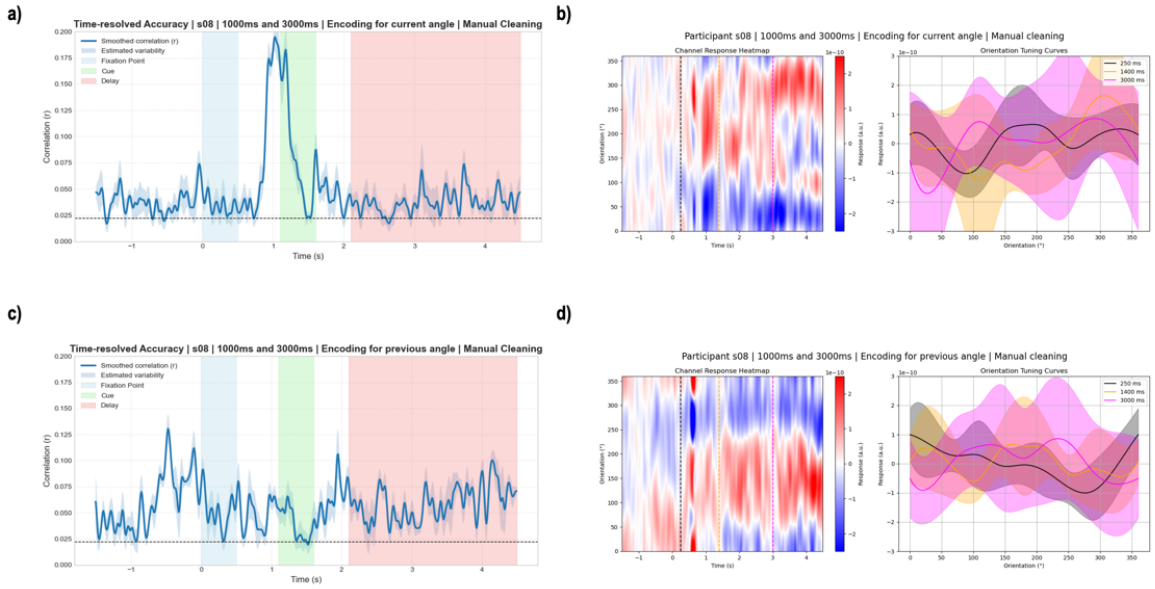

Figure 27. Forward encoding for subject s08's manual cleaning dataset. Where a) and c) represent the time-resolved accuracy during the decoding of the raw manually cleaned signal for the current and previous stimuli respectively. And b) and d) show the tuning curves of the model across time as a heatmap in the left panel, and as a time slice in the right panel. Each time slice corresponds to the dashed line in the heatmap.

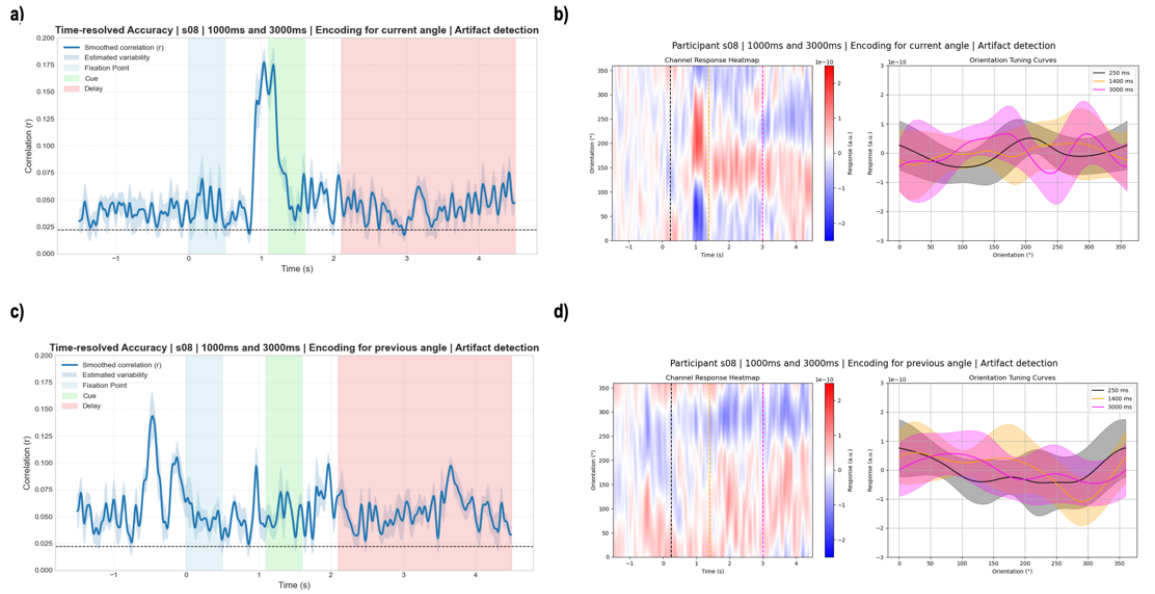

Figure 28. Forward encoding for subject s08's artifact detection dataset. Where a) and c) represent the time-resolved accuracy during the decoding of the raw artifact detection signal for the current and previous stimuli respectively. And b) and d) show the tuning curves of the model across time as a heatmap in the left panel, and as a time slice in the right panel. Each time slice corresponds to the dashed line in the heatmap.

Annex C. WBS Dictionary

WBS code	Package name
1.1	Background
Description	
Current state of research developed related with our project. Research on similar precedents to the proposed project. Where does the need to develop the project come from?	
Estimated time	5 days

WBS code	Package name
1.2	PERT
Description	
Definition of the agreed-upon times to be allocated to tasks. Determination of the project's critical path using PERT and forecast of its schedule in JIRA.	
Estimated time	4 days

WBS code	Package name
1.3	SWOT Diagram
Description	
Brief description of the specifications and technical features with the aim of studying the feasibility of carrying out the project. These specifications will be classified into what defines the strengths and weaknesses of the project, as well as its opportunities and threats.	
Estimated time	1 day

WBS code	Package name
1.4	WBS Dictionary
Description	
Document that divides and describes each work package at its minimum level and explains in detail how it should be done, with what criteria, and the appropriate deliverable. It will also include costs, delivery dates, and responsible parties.	
Estimated time	3 days

WBS code	Package name
1.5	Legal aspects
Description	
It involves addressing the legal considerations associated with conducting research involving human participants and handling sensitive medical data. It encompasses ensuring compliance with relevant laws, regulations, and ethical guidelines to protect the rights, privacy, and confidentiality of the participants and their data.	
Estimated time	2 days

WBS code	Package name
2.1	Installing necessary programs
Description	
This task involves the installation of software programs required for the project's execution. It includes identifying the specific programs needed based on project requirements and ensuring they are correctly installed on the relevant devices together with all their dependencies.	
Estimated time	1 day

WBS code	Package name
2.2	Setting up the cluster
Description	
The cluster will allow us to work with very heavy files for prolonged periods of time, in addition to offering large amounts of storage space which a computer would have not been able to handle.	
Estimated time	1 day

WBS code	Package name
3.1	Data acquisition
Description	
It consists of visiting the new hospitalized patients in the Unit of Epilepsy of the Hospital Clinic every 3 to 4 weeks to collect data. It is important to note that this process have been going on for a long time, although I have only been present for it for approximately 60 days.	
Estimated time	60 days

WBS code	Package name

4.1	Data organization
Description	
Organizing the acquired iEEG data into a structured format suitable for analysis, which corresponds to BIDS format. The organization process ensures that the data is ready for further analysis in subsequent tasks.	
Estimated time	5 days

WBS code	Package name
4.2	Electrode localization
Description	
Determining the precise localization of electrodes used for intracranial EEG (iEEG) measurements. This process includes identifying the specific brain regions or structures targeted by each electrode and mapping their coordinates within the brain. Electrode localization is essential for accurately interpreting the recorded neural activity and understanding its relationship to cognitive processes.	
Estimated time	30 days

WBS code	Package name
4.3	iEEG signal cleaning
Description	
Preprocessing and cleaning of the intracranial EEG (iEEG) signals obtained from patients with epilepsy. This process aims to enhance the quality of the recorded signals by removing noise, artifacts, and physiological interferences while retaining relevant neural activity. It is a core part of the project, as one of the objectives is to compare the results to a simple manual cleaning.	
Estimated time	60 days

WBS code	Package name
5.1	Univariate decoding analysis
Description	
Univariate decoding analysis aims to find the relation channel by channel to the participant's responses, this way it is possible to filter by channel significance (p-value) and localize particular brain areas participant in the working memory process.	
Estimated time	30 days

WBS code	Package name

5.2	Multivariate decoding analysis
Description	
During the multivariate decoding analysis, we will look on how the overall signal through all channels correlates to the responses.	
Estimated time	30 days

WBS code	Package name
5.3	Encoding analysis
Description	
Encoding analysis works the other way around, we will get accuracy reconstruction measures from responses to neural data and look for previous trial information reactivation in current trials.	
Estimated time	30 days

WBS code	Package name
5.4	Final results
Description	
Compiling, analyzing, and interpreting the results obtained from the research conducted on working memory, serial biases, and statistical learning. This task marks the culmination of data collection, processing, and analysis, providing insights into the relationship between these cognitive phenomena. The final results encompass findings, conclusions, and implications derived from the empirical research.	
Estimated time	5 days

Annex D. Participant consent form

CENTRO: Institut d'Investigacions Biomèdiques August Pi i Sunyer (IDIBAPS)
V4. 17/12/2018

Introducción

Nos dirigimos a usted para informarle sobre un estudio de investigación en el que se le invita a participar. El estudio ha sido aprobado por un Comité de Ética de la Investigación, de acuerdo a la legislación vigente, Ley de Investigación Biomédica 14/2007.
Nuestra intención es tan solo que usted reciba la información correcta y suficiente para que pueda evaluar y juzgar si quiere o no participar en este estudio. Para ello lea esta hoja informativa con atención y nosotros le aclararemos las dudas que le puedan surgir después de la explicación. Además, puede consultar con las personas que considere oportuno.

Participación voluntaria

Debe saber que su participación en este estudio es voluntaria y que **puede decidir no participar o cambiar su decisión y retirar el consentimiento en cualquier momento**.

Información general sobre el estudio

Con la finalidad de estudiar los mecanismos de la memoria de trabajo en el cerebro sano solicitamos su consentimiento para participar en un estudio que estamos llevando a cabo investigadores del Institut d'Investigacions Biomèdiques August Pi i Sunyer (IDIBAPS) y el Hospital Clínic.

El propósito de este estudio es investigar la relación entre percepción sensorial de estímulos débiles y su almacenamiento temporal en memoria de trabajo.
Entender los mecanismos de la capacidad cognitiva es importante para avanzar en posibles tratamientos para condiciones que la ven afectada.
Aunque este estudio no le va a aportar ningún beneficio directo a usted, puede servir para conocer mejor los mecanismos de la memoria en el cerebro, y a largo plazo podría beneficiar a otras personas.

¿Qué pasará durante el estudio?

Si decide participar en el estudio, participará en una sesión de aproximadamente una hora. Se le pedirá que lea y firme el consentimiento informado
En cada sesión, será sentado en un silla durante aprox. 60 min y se le pedirá que realice una tarea de memoria espacial muy sencilla de forma repetitiva.

Compensación económica

El promotor del estudio es el responsable de gestionar la financiación del mismo. Para la realización del estudio el promotor del mismo ha firmado un contrato con el centro donde se va a realizar y con el investigador responsable del estudio.
Su participación en el estudio no le supondrá ningún gasto. Para compensarle por su tiempo y por las molestias que le pueda causar su participación en el estudio, se ha establecido una compensación económica de 10€/hora que se le abonará tras su participación en el estudio mediante transferencia bancaria.

Confidencialidad

El Hospital Clínic de Barcelona, con CIF 0802070C, como responsable del tratamiento de

sus datos, le informa que el tratamiento, la comunicación y la cesión de los datos de carácter personal de todos los participantes se ajustará al cumplimiento del Reglamento UE 2016/679 del Parlamento Europeo y del Consejo de 27 de abril de 2016 relativo a la protección de las personas físicas en cuanto al tratamiento de datos personales y la libre circulación de datos, siendo de obligado cumplimiento a partir del 25 de mayo del 2018. La base legal que justifica el tratamiento de sus datos es el consentimiento que da en este acto, conforme a lo establecido en el artículo 9 del Reglamento UE 2016/679.
Los datos recogidos para estos estudios se recogerán identificados únicamente mediante un código, por lo que no se incluirá ningún tipo de información que permita identificar a los participantes. Sólo el médico del estudio y sus colaboradores con un permiso específico podrán relacionar sus datos recogidos en el estudio con su historia clínica.
Su identidad no estará al alcance de ninguna otra persona a excepción de una urgencia médica o requerimiento legal. Podrán tener acceso a su información personal identificada, las autoridades sanitarias, el Comité de Ética de Investigación y personal autorizado por el promotor del estudio, cuando sea necesario para comprobar datos y procedimientos del estudio, pero siempre manteniendo la confidencialidad de acuerdo a la legislación vigente.
Sólo se cederán a terceros y a otros países los datos codificados, que **en ningún caso contendrán información que pueda identificar al participante directamente (como nombre y apellidos, iniciales, dirección, número de la seguridad social, etc.)**. En el supuesto de que se produjera esta cesión, sería para la misma finalidad del estudio descrito y garantizando la confidencialidad.
Si se realizara una transferencia de datos codificados fuera de la UE, ya sea a entidades relacionadas con el centro hospitalario donde usted participa, a prestadores de servicios o a investigadores que colaboren con su médico, sus datos quedarán protegidos por salvaguardas como contratos u otros mecanismos establecidos por las autoridades de protección de datos.
Además de los derechos que ya contemplaba la legislación anterior (acceso, modificación, oposición y cancelación de datos, supresión en el nuevo Reglamento) ahora también puede limitar el tratamiento de datos que sean incorrectos, solicitar una copia o que se trasladen a un tercero (portabilidad) los datos que usted ha facilitado para el estudio. Para ejercitar estos derechos, o si desea saber más sobre confidencialidad, deberán dirigirse al investigador principal del estudio o al Delegado de Protección de Datos del Hospital Clínic de Barcelona a través de protecciodades@clinic.cat. Asimismo tienen derecho a dirigirse a la Agencia de Protección de Datos si no quedara satisfecho/a.
Los datos ya recogidos no se pueden eliminar aunque usted abandone el estudio, para garantizar la validez de la investigación y cumplir con los deberes legales y los requisitos de autorización de medicamentos. Pero no se recogerán nuevos datos si usted decide dejar de participar.

El Investigador y el Promotor están obligados a conservar los datos recogidos para el estudio al menos hasta 5 años tras su finalización. Posteriormente, la información personal solo se conservará por el centro para el cuidado de su salud y por el promotor para otros fines de investigación científica si el paciente hubiera otorgado su consentimiento para ello, y si así lo permite la ley y requisitos éticos aplicables.

CONSENTIMIENTO INFORMADO

Título del estudio: “Neural mechanisms underlying unconscious working-memory ”

Yo, (nombre del participante): .....
He leído la hoja de información general que se me ha entregado.
He leído las hojas de información sobre la EMT y entiendo los riesgos que puede tener.
He podido hacer preguntas sobre el estudio
He recibido suficiente información sobre el estudio
He recibido respuesta satisfactoria a mis preguntas
He hablado con (nombre del investigador): Leen Farrah / Alexis Pérez Bellido

Comprendo que mi participación es voluntaria

Comprendo que puedo retirarme del estudio:

1. Cuando quiera
2. Sin tener que dar explicaciones

Consiento que los posibles resultados obtenidos con mi participación en el estudio sean fuente de publicaciones científicas, siempre que se vele por mi completo anonimato.

Presto libremente mi conformidad para participar en el:
☐ Experimento 1: estudio cognitivo

Firma del participante: Firma del investigador:

Lugar y fecha:

Annex E. iEEG processing, cleaning and analysis code

Since the code is too long for these annexes, the full preprocessing and analysis pipeline is publicly available as a GitHub repository at: https://github.com/AlbertoHurtadoMorell/iEEG_Cleaning_Analysis